Energy transfer between short wave groups and bound long waves on a plane slope



J.C. van Noorloos
June 2003

MSc Thesis

Delft University of Technology
Faculty of Civil Engineering and Geosciences
Section of Fluid Mechanics

TU Delft

©2003. J.C. van Noorloos

Energy transfer between short wave groups and bound long waves on a plane slope

MSc Thesis
Job C. van Noorloos
June 2003



Thesis committee:
Prof. dr. ir. J.A. Battjes
Dr. ir. A.R. van Dongeren
Dr. ir. A.J.H.M. Reniers
Ir. T.T. Janssen

Preface

This thesis is submitted in conformity with the requirements for the degree of Master of Science in Civil Engineering. For the present research, experiments were carried out in the Laboratory of Fluid mechanics at Delft University of Technology. The project was fulfilled under supervision of Prof. dr. ir. J.A. Battjes. I want to thank him for the detailed comments on the report, as well as the guidance and support during the past 8 months.

I would like to thank Ap van Dongeren for his numerous visits payed to room 2.92. His explanations concerning surf-beat and everything around it helped a great deal in the process of understanding.

I want to thank Tim Janssen for his enthusiasm and support. Although he stayed in the USA during almost the whole project, he helped a great deal by means of e-mail and phone calls. In addition to the usefulness, I appreciate his view and comments on graduation in general.

Ad Reniers I would like to thank for the hours spent debugging on my behalf. It helped a great deal improving the measurement results and the understanding of the decomposition method. Gert Klopman for disposing his time for helping me with decomposition problems and provision of some useful Matlab scripts.

I will thank Elselien for her unlimited support and energy both metaphorically and literally (at least concerning the energy part) and Matthijs van Baarsel for the unique cartoon.

Furthermore I would like to thank al who have contributed to this thesis, and especially everybody who did this by means of dropping by for a cup of coffee. I probably enjoyed that more than you can imagine.

Job C. van Noorloos
(Delft 2003)

Abstract

The present report describes a laboratory study on energy transfer between short wave groups and bound long waves. From previous experiments (Battjes et al. (2003)) the bound wave travelling shoreward is observed to grow faster than Green's Law, indicating that the bound wave gains energy from other spectral components. Under certain conditions, specific low-frequency components show growth equal to the equilibrium response ($\propto h^{-5/2}$), as was presented by Longuet-Higgins and Stewart (1962).

In addition to the above observations, laboratory experiments were performed. The observations are compared with an energy model transfer model enabling energy transfer from high frequency waves (HF) to low-frequency waves. To obtain quasi-continuous estimations of the bound wave amplitude, high resolution 2-D laboratory data is obtained for several (both bound wave frequency varying and modulation varying) bichromatic and irregular wave fields. The test were performed on a plane sloping (1:35) beach.

Based on existing models concerning surfbeat generation a testprogramme is designed to determine a criterion for the beach slope being 'gentle' or 'steep' for long wave frequencies. The analysis of the acquired data comprises long wave decomposition into incoming and outgoing waves. The decomposition method presented by Bakkenes (2002) is extended with two iteration steps. Phase analysis of the incoming bound wave and incoming HF wave groups shows an increasing phase lag of the bound wave after the wave groups. This phase lag is used in the energy transfer model. Comparison to the predicted values of the model with (decomposed) observations shows very good agreement for the incoming LF waves, but large deviations for the outgoing LF waves. Furthermore, the amplitude growth of the incoming bound long wave is compared with the 'equilibrium response growth' and related to the normalized bed slope β as an indication whether the equilibrium response is to be expected. From the present observations it is concluded that a lower value of β gives a good indication for the *energy transfer* rather than for the amplitude growth; for higher subharmonic frequencies significant energy dissipation occurs, preventing the LF wave to grow as expected based on the β variation. The varying modulation does not lead to different amplitude behavior.

The outgoing wave amplitude is observed to be highly dependent of the bound wave frequency. In specific cases, the outgoing amplitude exceeds the incoming amplitude. No conclusions are drawn concerning the processes governing the reflection.

Contents

Preface **v**

Abstract **vii**

List of Tables **xii**

List of Figures **xii**

List of Symbols **xiv**

1 Introduction **1**
1.1 General . . . 1
1.2 Outline . . . 2

2 Wave theory **3**
2.1 Linear wave theory . . . 3
2.1.1 Energy . . . 5
2.1.2 Energy flux . . . 5
2.1.3 Radiation stress . . . 6
2.1.4 Shoaling of free waves . . . 7
2.2 Long waves . . . 7
2.2.1 Generation . . . 8
2.2.2 Shoaling . . . 8
2.2.3 Free long wave generation . . . 10

3 Experimental setup **13**
3.1 Previous work . . . 13
3.2 Objectives . . . 13
3.3 Physical setup . . . 14
3.3.1 Wave gauges . . . 14
3.3.2 EMS . . . 16
3.3.3 Video . . . 16
3.3.4 Data-acquisition . . . 17
3.4 Testprogramme . . . 17

3.4.1 Bichromatic wave experiments . . . 18
3.4.2 Irregular wave experiments . . . 20

4 Data analysis **21**
4.1 Data preparation . . . 21
4.1.1 Composition of simultaneous time series . . . 21
4.1.2 Wave reproduction . . . 22
4.2 Decomposition . . . 23
4.2.1 General . . . 23
4.2.2 Horizontal case . . . 24
4.2.3 Sloping case . . . 27
4.2.4 First calculation . . . 28
4.2.5 Second calculation . . . 30
4.2.6 Third calculation . . . 31
4.3 EMS data . . . 32
4.4 Phaselagging . . . 33

5 Analysis results **36**
5.1 Incoming waves . . . 36
5.1.1 Observations . . . 36
5.1.2 Model comparison . . . 38
5.2 Outgoing waves . . . 40
5.2.1 Observations . . . 40
5.2.2 Model comparison . . . 40
5.3 Evaluation of testprogramme . . . 41

6 Conclusions and Recommendations **44**
6.1 Conclusions . . . 44
6.2 Recommendations . . . 44

Bibliography **46**

A Wave envelope **48**
A.1 Hilbert transformation . . . 49

B Windowing **51**

C Data acquisition **53**
C.1 Experiments . . . 53

D Graphics **56**
D.1 HF wave decomposition . . . 56
D.2 3-D representation of spatial evolution of amplitude spectra . . . 58
D.3 Overview of analysis . . . 59

D.4 Reflection plots 67

List of Tables

3.1 Parameters of bichromatic experiments 19
3.2 Frequencies of bichromatic series in terms of multiples of the basic frequency f_0. 19
3.3 Wave parameters, series C and D. 20

4.1 Results of decomposition of wave signal. 27
4.2 Amplitude target values and measured values for primary and bound components. 29

List of Figures

2.1 Directions and variables 4
2.2 Wave grouping and amplitude envelope 6
2.3 Linear dispersion relation for depth of 0.7 m. 9
2.4 Breakpoint generation model. 11
2.5 Time varying and fixed breakpoint characteristics 12

3.1 Bathymetry and flume dimensions 14
3.2 Gauges in shallow water. 15
3.3 Gauge locations in horizontal and sloping case. 16
3.4 Wave gauge and EMS 17

4.1 Amplitude spectra for series A-4. 22
4.2 Wave reproduction. 23
4.3 Shifted reference gauge time series for D-3 experiments. 24
4.4 Critical gauge spacing. 24
4.5 Measurement setup 25
4.6 Amplitude spectra for incoming and outgoing free HF waves 26
4.7 Reflection coefficients for the used wave generator. 28
4.8 Test results of decomposition, sloping case, step one 30
4.9 Test results of decomposition, sloping case, step two 31
4.10 Test results of decomposition, sloping case, step three 32
4.11 Test results of decomposition, sloping case, iteration step two. Polluted signal. 33
4.12 Results of EMS decomposition, sloping case 34
4.13 Phase lag, work and amplitudes of series B-2 35

5.1 Amplitudes of incoming LF waves, series A and B. 36
5.2 Normalized amplitudes for series A and B (right). 37
5.3 Phase differences between incoming short wave envelope and incoming bound long wave . . 38
5.4 Work done on the incoming LF waves for series A and B 39
5.5 Observed and computed incoming LF wave amplitudes 39
5.6 Observed outgoing LF wave amplitudes 40
5.7 Incoming and outgoing amplitudes for series B-2 and B-5 41
5.8 Phase difference between incoming short wave envelope and outgoing LF wave 41

5.9 Observed and computed outgoing LF wave amplitudes for series A-1 and B-3 42
5.10 Observed and computed incoming bound wave amplitudes 42

A.1 Amplitude determination 48
A.2 Fourier series of bichromatic signal 50
A.3 Fourier series of shifted bichromatic signal. 50

B.1 Spectral windows for rectangular and Hanning time windows 51

C.1 Contents of structural array 53
C.2 4 wave gauge amplifiers. 54
C.3 Data acquisition hardware: computer and 16-channel DAP-box 54

D.1 Results of HF wave decomposition 56
D.2 Results of HF wave decomposition 57
D.3 3-D amplitude spectra for series A. 58
D.4 Compilation of series A-1 59
D.5 Compilation of series A-2 60
D.6 Compilation of series A-3 61
D.7 Compilation of series A-4 62
D.8 Compilation of series B-2 63
D.9 Compilation of series B-3 64
D.10 Compilation of series B-4 65
D.11 Compilation of series B-5 66
D.12 Incoming and outgoing amplitude for series A-1 trough A-4. 67
D.13 Incoming and outgoing amplitude for series B-2 trough B-5. 68

List of Symbols

LATIN	
a	amplitude
a_n	amplitude of component n
a_{in}	amplitude of incoming free wave
a_{out}	amplitude of outgoing wave
a_{bo}	amplitude of incoming bound wave
$\hat{a}_\infty$	deep water wave steepness
c	phase speed
c_d	deep water phase speed
c_s	shallow water phase speed
c_g	group speed
c_{g0}	deep water group speed
C_{xy}	normalized cross-covariance
E_k	kinetic energy
E_t	total mean wave energy
f_0	basic frequency in Fourier transformations
f_s	sampling frequency
f_N	Nyquist frequency
F	energy flux
g	acceleration of gravity
h	water depth
h_b	breaking depth
h_x	beach slope $\frac{\mathrm{d}h}{\mathrm{d}x}$
H	wave height
HF	high frequency
$_j$	frequency counter
k	free wave number
k_{bo}	bound wave number
K_s	shoaling factor
L	wavelength
LF	low frequency

LATIN(continued)

m	time lag
n	depth number
N	number of samples
p	pressure
$_p$	location counter
S_{xx}	radiation stress
S_j	radiation stress of jth frequency component
t	time
T	wave period
T_p	peak period
T_r	duration of time record
u	particle velocity in x-direction
x	horizontal spatial variable
X	slowly varying space scale
z	vertical spatial variable

GREEK

α	van Dongeren parameter
β	normalized bed slope
γ	breaking parameter
δ	modulation
η	surface elevation
$\overline{\eta}$	time averaged surface elevation
κ	Schäffer parameter
ξ_j	(real) amplitude of jth frequency component
ρ	density
ϕ	velocity potential
$\Phi_{j,p}$	phase
ω	angular frequency
ω_j	jth angular frequency component
χ	Symonds parameter

Chapter 1

Introduction

1.1 General

The present thesis deals with a laboratory study about a wave phenomenon caused by a slow amplitude variation of wind waves. Wind waves, or short waves, have a period of about 2-20 seconds. For narrow-banded wave trains, the time scale of the variation of amplitude is much larger; about 20-100 seconds. On the larger timescale oscillations can be observed in the nearshore zone. This phenomenon is called *surfbeat*. Surfbeat was first reported by Munk (1949) and Tucker (1950), and subject of various studies since then. The importance of gaining more insight in the surf beat generation process becomes clear when considering that

- surf beat frequencies in the nearshore zone are relatively energetic, thus important in coastal morphodynamic processes,
- surf beat may cause resonant excitation of (large-)vessel systems which is, of course, highly unfavorable,
- surf beat results in slowly varying depth, which can be crucial in designing shore protection works.

As a result of the studies conducted, several surfbeat generation models have been proposed. Biésel (1952) and, independently, Longuet-Higgins and Stewart (1962) presented a mechanism for the occurrence of low frequency waves, based on non-linear wave interactions. Their, now widely used, concept is valid on horizontal bathymetry, but application in regions with varying depth is not straightforward. A model focused on the low frequency (LF) wave generation in the nearshore zone, taking depth variation into account, was presented by Symonds et al. (1982). In this model long waves are generated by the movement of the breakpoint of the short waves. Enhancements to this model were presented by Schäffer and Svendsen (1988) by keeping the point of initial breaking fixed. Surf beat is than generated *in* the surf zone. Schäffer (1993) combines the fixed and moving breakpoint mechanisms.
Laboratory experiments focused on energy transfer are few. Kostense (1984) generated bound waves, but performed measurements on the horizontal part of the flume only. Baldock et al. (2000) and Baldock and Huntley (2002) show the presence of breakpoint generated waves on a relatively steep (plane) slope and with bound wave frequencies even larger than the primary frequencies. Janssen et al. (2003) analyzed laboratory data of Boers (1996) and found no evidence for the presence of breakpoint generated waves.

The relevance of the mechanisms is discussed in Van Dongeren et al. (2002). Battjes et al. (2003) observed a frequency dependence of the growth of the bound wave travelling shoreward; higher frequency bound waves were observed to behave nearly according to the equilibrium model presented by Longuet-Higgins and Stewart (1962).
As stated before, laboratory experiments concerning this subject are few. Recent observations (Battjes et al. (2003) lead us to the need of verification by laboratory experiments and to the following goals for this thesis:

- acquire high quality laboratory data, primarily focused on the spatial evolution of the system of bound waves and short wave groups on the slope,
- compare the observed amplitude behavior with the results of an energy transfer model,
- determination of a criterion, when the bound wave growth corresponds with equilibrium response.

1.2 Outline

Chapter 2, focuses on the theoretical basis needed throughout this thesis, e.g. linear wave theory and radiation stress. A summary of relevant parameters is presented. Chapter 3, Experimental setup, uses these parameters in the testprogramme design and discusses the physical setup and measurement procedures as well as previously performed tests. The data obtained by the laboratory experiments are analyzed in Chapter 4. The measured wave signal is decomposed into several directional components (shoreward and seaward propagating waves) by different decomposition techniques. Decomposition of a signal into free and bound wave contributions makes further analysis possible. Visualization of changing properties by means of cross-correlation and the calculation of the phase lag between the bound wave and the short wave envelope is also subject of Chapter 4. Chapter 5 presents the interpretation of the analyzed data. The variation of phase, amplitude and energy transfer is emphasized and related to the parameters from the testprogramme. Finally, Chapter 6 presents conclusions and recommendations for further work. For more detailed information regarding to the data acquisition in this thesis, reference is made to Appendix C.
All analysis procedures are performed through Matlab scripts. Where applicable references are made to specific scripts by means of footnotes. Anyone interested in these scripts or a digital version of this thesis can obtain them freely by mailing to v_noorloos@hotmail.com.

Chapter 2

Wave theory

As a basis for the following chapters the present chapter deals with the basic concepts of wave theory Extensive descriptions of this subject can be found in e.g. Dean and Dalrymple (1984) and Battjes (2001).

2.1 Linear wave theory

We write the following set linearized equations (e.g. Battjes, (2001)) and boundary conditions are read to describe two-dimensional fluid motion on a horizontal bottom

$$\frac{\partial^2 \phi}{\partial x^2} + \frac{\partial^2 \phi}{\partial z^2} = 0, \tag{2.1}$$

$$\frac{\partial \phi}{\partial z} = \frac{\partial \eta}{\partial t} \qquad \text{and} \qquad \frac{\partial \phi}{\partial t} + g\eta = 0 \qquad \text{at} \qquad z = 0, \tag{2.2}$$

$$\frac{\partial \phi}{\partial z} = 0 \qquad \text{at} \qquad z = -h, \tag{2.3}$$

where ϕ is the velocity potential, x the horizontal coordinate, z the vertical coordinate pointing up from the free surface, g the acceleration of gravity, t the time and h the water depth (for definitions see Figure 2.1). Equation (2.1) is known as the Laplace equation. The above set of equations is obtained upon assuming that the amplitude a of the surface elevation η is small compared to the depth h and wavelength L. In other words, the linear approximation assumes a weakly disturbed surface.
Solving the Laplace equation (2.1) for a sine wave propagating in positive x-direction with wave height H, period T and wavelength L (see Figure 2.1), we write for η

$$\eta(x,t) = \frac{1}{2} H \sin\left(\frac{2\pi t}{T} - \frac{2\pi x}{L}\right). \tag{2.4}$$

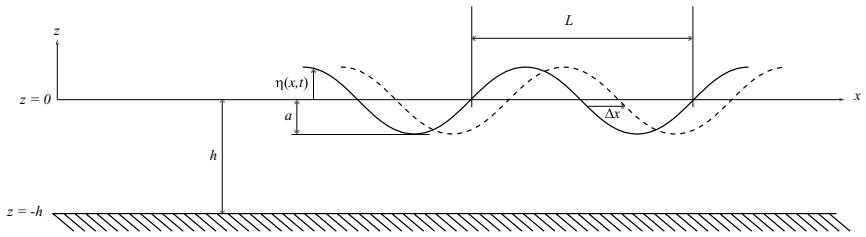


Figure 2.1: Directions and variables. The dotted line represents the surface elevation on $t = t + \Delta t$.

For convenience we define

$$\begin{aligned} \text{amplitude } a &= \frac{1}{2}H, \\ \text{angular frequency } \omega &= \frac{2\pi}{T}, \\ \text{wave number } k &= \frac{2\pi}{L}, \end{aligned} \tag{2.5}$$

and (2.4) can be written

$$\eta(x,t) = a\sin\left(\omega t - kx\right). \tag{2.6}$$

The phase speed c of this wave can be expressed as

$$c = \frac{\omega}{k} = \frac{L}{T}. \tag{2.7}$$

Solving the Laplace equation (2.1) for (2.6) with above boundary conditions (2.2) and (2.3) leads to

$$\phi(x,z,t) = \frac{\omega a}{k}\frac{\cosh(k(h+z))}{\sinh(kh)}\cos(\omega t - kx). \tag{2.8}$$

Substitution of (2.8) in the set (2.2) yields

$$\omega^2 = gk\tanh(kh). \tag{2.9}$$

This relation between wavenumber and frequency is often referred to as the linear dispersion relation for free surface gravity waves [1]. The dispersion relation determines the speed of disturbance propagation in a certain region for a given frequency. Substitution of the dispersion relation in (2.7) leads to

$$c^2 = \frac{w^2}{k^2} = \frac{g}{k}\tanh kh, \qquad \text{or} \qquad c = \sqrt{\frac{gL}{2\pi}\tanh\frac{2\pi h}{L}}. \tag{2.10}$$

Using the properties of the hyperbolic functions in (2.10) this equation can be simplified for certain relative depth regions (expressed by the kh-factor). The wave propagation velocity c_d for relatively deep water ($kh \gg 1$), thus $\tanh kh \approx 1$, becomes then

$$c_d \approx \frac{g}{\omega}. \tag{2.11}$$

[1] Matlab-script `dispergk.m`

In shallow water where $kh \ll 1$, thus $\tanh kh \approx kh$, k can be eliminated from (2.9) and (2.7) and the velocity c_s can be derived

$$c_s = \sqrt{gh}. \tag{2.12}$$

2.1.1 Energy

The energy in a wave field consists of two parts, the kinetic energy and the potential energy. The mean kinetic energy E_k can be expressed as

$$E_k = \frac{1}{2}\rho \overline{\int_{-h}^{\eta} |\mathbf{u}|^2 dz}, \tag{2.13}$$

with $\mathbf{u} = [\frac{\partial \phi}{\partial x}, \frac{\partial \phi}{\partial z}]$; assuming the disturbance to be of small amplitude, we write (2.13) as

$$E_k = \frac{1}{2}\rho \int_{-h}^{0} \overline{|\mathbf{u}|^2} dz, \tag{2.14}$$

and upon substituting $\frac{\partial \phi}{\partial x}$ and $\frac{\partial \phi}{\partial z}$ we find

$$E_k = \frac{\rho(\omega a)^2}{4k} \coth kh. \tag{2.15}$$

Upon applying (2.9), (2.15) reduces to

$$E_k = \frac{1}{4}\rho g a^2. \tag{2.16}$$

In a conservative dynamic system with small oscillations the mean kinetic energy is equal to the mean potential energy. This leads to the following expression for the total mean energy per unit of surface area E_t,

$$E_t = 2E_k = \frac{1}{2}\rho g a^2. \tag{2.17}$$

2.1.2 Energy flux

The mean rate of energy transfer F of waves parallel to the direction of propagation can be written

$$F = Enc, \qquad \text{with} \qquad n = \frac{1}{2} + \frac{kh}{\sinh 2kh}. \tag{2.18}$$

The dimensionless parameter n depends only on kh, and thus the relative depth. The velocity at which the energy of a certain wave field, the wave front, propagates in a (not necessarily) undisturbed region is expressed by

$$c_g = \frac{\partial \omega}{\partial k} = nc, \tag{2.19}$$

where c_g is called the group speed. This implies that individual wave crests travel with a relative velocity $(c - nc)$ with respect to the envelope (see Figure 2.2). It follows from (2.19) that the group speed c_g varies between 0.5 and 1 times the phase speed for deep and shallow water respectively; i.e. in shallow water the group speed equals the phase speed, while in deep water the group speed equals half the phase speed. The concept of wave grouping is visualized in Figure 2.3.

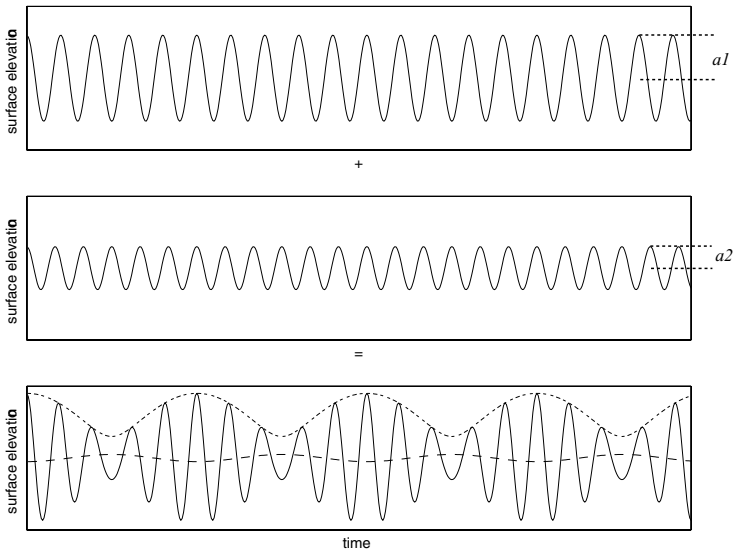


Figure 2.2: Upper two panels show the primary waves (solid lines), the lowest panel shows the superposition of the two primary waves and the amplitude envelope (upper dashed line) obtained by Hilbert transformation (see section A.1). The dash-dot line represents the bound long wave

2.1.3 Radiation stress

The concept of radiation stress was introduced by Longuet-Higgins and Stewart (1962). Physically, radiation stress is the excess transport of horizontal momentum due to the presence of waves. The total momentum transport through a vertical plane per unit width in water with depth h and surface elevation η consists of two parts. An advection component, which can be written

$$\int_{-h}^{\eta} \rho u^2 dz, \tag{2.20}$$

and a pressure component, which can be written

$$\int_{-h}^{\eta} p dz, \tag{2.21}$$

where p represents the pressure, u the horizontal particle velocity and ρ the density of the fluid. Adding these contributions and time-averaging over an integer number of wave periods yields

$$\overline{\int_{-h}^{\eta} (p + \rho u^2) dz}. \tag{2.22}$$

The overline denotes the time averaging operation. The excess momentum transport due to the waves is determined by subtracting the transport of momentum without waves yielding

$$S_{xx} \equiv \overline{\int_{-h}^{\eta} (p + \rho u^2) dz} - \int_{-h}^{0} p_0 dz. \tag{2.23}$$

Applying linear theory, the following expression can be found for S_{xx}:

$$S_{xx} = E\left(\frac{2kh}{\sinh(2kh)+\frac{1}{2}}\right) \qquad \text{or} \qquad S_{xx} = E(2n-\frac{1}{2}). \tag{2.24}$$

2.1.4 Shoaling of free waves

Considering cross-shore energy flux on a sloping beach, uniform in alongshore direction, while assuming negligible dissipation, the energy flux F must remain constant; i.e F =constant in cross-shore direction. In terms of amplitude this can be written as

$$\frac{F_1}{F_2} = \frac{E_1 c_{g1}}{E_2 c_{g2}} = 1 \Rightarrow \frac{a_2}{a_1} = \sqrt{\frac{c_{g1}}{c_{g2}}}, \tag{2.25}$$

where subscripts denote a cross-shore position. For shallow water ($c_g \approx \sqrt{gh}$) it can be seen that the amplitude varies proportional to $h^{-\frac{1}{4}}$. This shoaling behavior is often referred to as Green's Law. With a reference point located on deep water, denoted by 0 as subscript, we can define a shoaling factor K_s

$$K_s \equiv \sqrt{\frac{c_{g0}}{c_g}}. \tag{2.26}$$

2.2 Long waves

This section focuses on low frequency (LF) waves and describes various theories concerned with the generation, shoaling and 'releasing' mechanisms of these low frequency (long) waves. Assume the length of a wave group long compared to the depth. This allows us to depth and time average the conservation equations governing the motion of the fluid. For a one-dimensional situation (e.g. a flume) these equations for mass and momentum conservation can be written as (e.g. Schäffer (1993))

$$\frac{\partial \overline{\eta}}{\partial t} + \frac{\partial}{\partial x}((h+\overline{\eta})U) = 0, \tag{2.27}$$

$$\frac{\partial U}{\partial t} + U\frac{\partial U}{\partial x} + g\frac{\partial \overline{\eta}}{\partial x} = \frac{-1}{\rho(h+\overline{\eta})}\frac{\partial S_{xx}}{\partial x}, \tag{2.28}$$

where $\overline{\eta}$ is the surface elevation averaged over the short wave period and U is the corresponding depth averaged long wave particle velocity. The above equations are the non-linear shallow water equations with a forcing term and change into linear equations when $|\overline{\eta}| \ll h$ is assumed. In that case the linearized equations read

$$\frac{\partial \overline{\eta}}{\partial t} + \frac{\partial}{\partial x}(hU) = 0, \tag{2.29}$$

$$\frac{\partial U}{\partial t} + g\frac{\partial \overline{\eta}}{\partial x} = \frac{-1}{\rho h}\frac{\partial S_{xx}}{\partial x}. \tag{2.30}$$

2.2.1 Generation

When evaluating a situation with a horizontal bottom, (2.29) can be written as

$$\frac{\partial \overline{\eta}}{\partial t} + h\frac{\partial U}{\partial x} = 0. \tag{2.31}$$

The amplitude modulations travel with the group velocity c_g, hence the $\frac{\partial}{\partial t}$ term can be replaced with $-c_g\frac{\partial}{\partial x}$. The following expressions can be obtained

$$-c_g\frac{\partial \overline{\eta}}{\partial x} + h\frac{\partial U}{\partial x} = 0, \qquad \text{and} \tag{2.32}$$

$$-c_g\frac{\partial U}{\partial x} + g\frac{\partial \overline{\eta}}{\partial x} = \frac{-1}{\rho h}\frac{\partial S_{xx}}{\partial x}. \tag{2.33}$$

Elimination of U and integrating with respect to x yields the surface elevation of the long wave motion

$$\overline{\eta} = -\frac{S_{xx}}{\rho(gh - c_g^2)} + C, \tag{2.34}$$

where integration constant C may be chosen as zero arbitrarily. This means that the LF surface elevation is negatively correlated with the local short wave amplitude. This can be understood by considering $-\frac{\partial S_{xx}}{\partial x}$ as a pressure applied on the water. It can be seen from (2.34) that if the group speed c_g approaches the shallow water limit, $\sqrt{gh}$, the denominator approaches zero and $\overline{\eta}$ will become unbounded. Due to the breaking process the short waves will not reach the very shallow parts of a slope in practice but for shallow water $c_g^2 \approx gh[1 - (kh)^2 + O(kh)^4]$ can be adopted and (2.34) can be written as

$$\overline{\eta} \approx \frac{-S_{xx}}{\rho g h (kh)^2}. \tag{2.35}$$

It can be seen from (2.10) that $k^2 = \frac{\omega^2}{gh} + O((kh)^2)$ and (2.35) changes into

$$\overline{\eta} = \frac{-S_{xx}}{\rho\omega^2 h^2} = -\frac{3ga^2}{4\omega^2 h^2}. \tag{2.36}$$

The relation of the bound wave with the short waves can be visualized in a graph of the dispersion relation. (Figure 2.3, left panel). Note the different gradients ($c_g = \frac{\partial \omega}{\partial k}$) of the lines 1, 2 and 3.

2.2.2 Shoaling

The previous section dealt with generation on a horizontal bottom. The present section tries to shed some light on the shoaling properties of bound waves and the difficulties that may arise when performing laboratory tests.

Adopting a quasi-uniform approach, we assume that the beach slope h_x is small enough for the equilibrium between forcing and response to be established. The variation of S_{xx} along the slope is to be described first. Since the incoming short wave amplitude in shallow water increases with decreasing depth according $a \propto h^{-\frac{1}{4}}$, the radiation stress S_{xx} behaves like $S_{xx} \propto h^{-\frac{1}{2}}$. Then, still under the shallow water assumption, (2.34) is valid and it can be seen that the bound wave amplitude $\overline{\eta}$ varies according $\overline{\eta} \propto h^{-\frac{5}{2}}$. It should be noted that this is only the case when the dynamic equilibrium can be established, which is partly subject of this study.

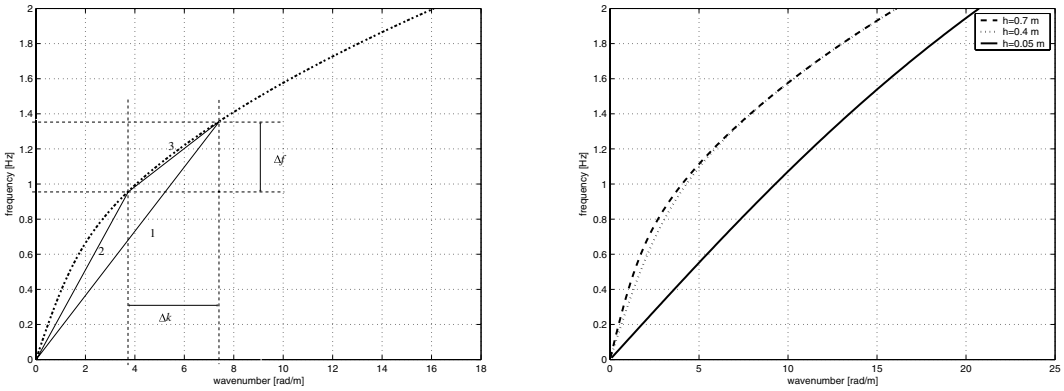


Figure 2.3: Left panel: Linear dispersion relation for depth of 0.7 m.(dashed line). Solid lines 1 & 2 represent primary free wave dispersion, 3 represents the dispersion relation of the bound long wave. Right panel: dispersion relation for three depths; the solid line (shallow water) shows an almost linear behavior, resulting in almost identical propagation speed ($\frac{\mathrm{d}\omega}{\mathrm{d}k} \approx \sqrt{gh}$) for the primary and bound wave components .

Janssen et al. (2003) find a solution of the linearized shallow water equations (2.29) and (2.30). Combination of (2.29) and (2.30) yields

$$\frac{\partial}{\partial x}\left(gh\frac{\partial}{\partial x}\overline{\eta}\right) - \frac{\partial^2\overline{\eta}}{\partial t^2} = -\frac{1}{\rho}\frac{\partial^2 S_{xx}}{\partial x^2}, \tag{2.37}$$

where $\overline{\eta}$ represents the LF surface elevation. Assuming $\overline{\eta}$ to be a summation of plane waves, we can write it as

$$\overline{\eta} = \sum_{n=1}^{m} \frac{1}{2}\xi_n e^{-i\omega_n t} + *, \tag{2.38}$$

where the $*$ denotes the complex conjugate of the preceding term, ξ_n is the complex amplitude of the nth component and ω_m the cut-off frequency for LF-motion. Using this, (2.37) can be expressed as

$$gh\frac{\mathrm{d}^2}{\mathrm{d}x^2}\xi_n + g\frac{\mathrm{d}h}{\mathrm{d}x}\frac{\mathrm{d}}{\mathrm{d}x}\xi_n + \omega^2\xi_n = -\frac{1}{\rho}\frac{\mathrm{d}^2 S_n}{\mathrm{d}x^2}, \tag{2.39}$$

where S_n denotes the n-th component of the Fourier transformed radiation stress S_{xx}. A scaling parameter β can be introduced, known as the normalized bed slope

$$\beta = \frac{\mathrm{d}h/\mathrm{d}x}{kh}, \tag{2.40}$$

with

$$k = \frac{\omega}{c_g} \qquad \text{and} \qquad c_g = \sqrt{gh}, \tag{2.41}$$

(2.40) can be written as

$$\beta = \frac{h_x}{\omega}\sqrt{\frac{g}{h}}. \tag{2.42}$$

2.2.3 Free long wave generation

When the short wave groups propagate shoreward the amplitude will increase and the wavelength will shorten until the the waves become too steep. Considering a gentle slope the HF waves break relatively far from the shoreline and dissipate energy over this distance. As a result, the short waves almost fully disappear without reflection, while the LF wave may be long enough to be reflected by the slope. Since the short wave energy decays, the bound long wave becomes more and more a free wave and propagates accordingly. Several theories have been proposed about this so-called release process.

Time varying breakpoint

Symonds et al. (1982) present a model for the generation of free LF waves caused by the variation of the breakpoint positions due to groupiness. The higher waves break further offshore, the smaller waves closer to shore, so the breakpoint moves with a frequency equal to the group frequency. The breaking of the primary waves is determined by the breaking depth h_b.

$$h_b = \frac{a(t)}{\gamma}, \tag{2.43}$$

where $a(t)$ is the amplitude of the primary wave and γ the breaking constant, taken 0.4 within the surf zone similar to Symonds et al. (1982). It is assumed that no groupiness will occur in the surf zone and the water level will vary with the group frequency. This variation was presented by Longuet-Higgins and Stewart (1962) and can be considered as LF motion in case of irregular wave groups breaking on a beach. In Symonds et al. (1982) the linear shallow water equations (2.29) and (2.30) are made non-dimensional by dividing by their mean values. The point of initial breaking acts like a wave generator radiating LF waves in both seaward and shoreward direction. The shoreward propagation waves are assumed to be totally reflected at the shoreline, which results in a standing wave pattern. After reflection at the shoreline this (now seaward propagating) wave will, depending on the relative phase, coincide with the directly seaward radiated wave. The phase difference depends on the dimensionless parameter χ defined as

$$\chi \equiv \frac{\omega^2 h_b}{g h_x^2}, \tag{2.44}$$

where ω is the group frequency, h_b the depth at the mean breakpoint position, g the acceleration of gravity and h_x the beach slope. The relation with the resulting outgoing wave amplitude is shown in Figure 2.4. It is noted that this approach neglects the incoming bound wave.

Fixed breakpoint

Another approach is the fixed breakpoint theory which was presented by Schäffer and Svendsen (1988). In contrast to the model of Symonds et al. (1982), they propose a fixed breakpoint position and let the groupiness propagate into the surfzone. The differences are sketched in Figure 2.5.
A hybrid model is proposed by Schäffer (1993). It combines the time-varying and the fixed breakpoint mechanism. A weighting parameter κ gives the relative importance of the two concepts. For a bichromatic

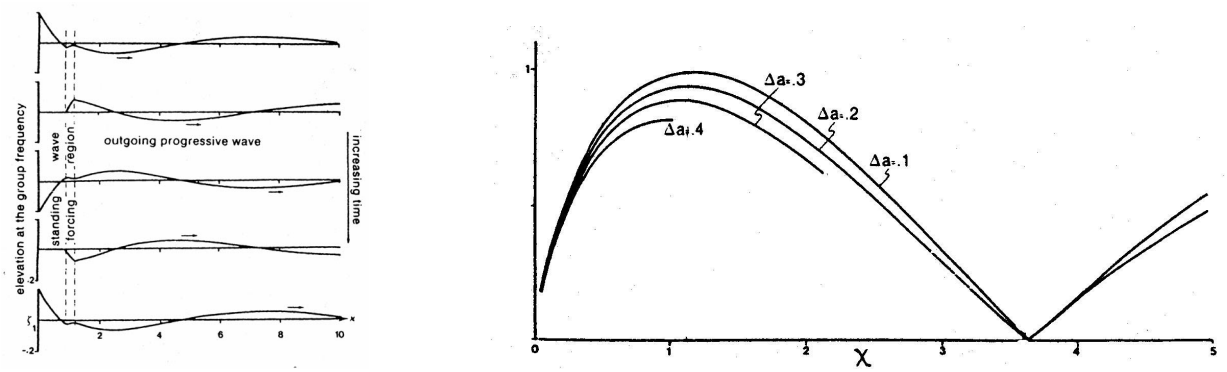


Figure 2.4: Left panel: Solutions for elevation at different stages of a group period. Right panel: Normalized amplitude of outgoing free wave versus χ (reprinted from Symonds et al. (1982)) .

signal this approach yields for the surf zone amplitude A

$$|A|^2 = \gamma^2 \left[1 + (1-\kappa)2\delta \cos \Delta\omega + O(\delta^2)h^2\right], \tag{2.45}$$

where δ represents the modulation of the primary waves (see Figure 2.2 for definition of δ), $\Delta\omega$ the group frequency and h the water depth. For $\kappa = 0$ the model is simplified to a fixed break-point model with full transmission of groupiness into the surf zone. For $\kappa = 1$ the model equals the time varying model of Symonds et al. (1982). The value of κ is derived from the relation between breaking parameter γ and the deep water wave steepness $\hat{a}_\infty$ for a certain bed slope. This results in

$$\kappa = 1 - \frac{\partial \log \gamma}{\partial \log \hat{a}_\infty}. \tag{2.46}$$

The second term on the right hand side of (2.46) appears to be zero or negative indicating that we always have $\kappa \geq 1$. Using data obtained by Hansen (1990) results in a constant value $\kappa = 1.09$. A value larger than 1 represents a reversal of grouping as the short waves pass through the zone of initial breaking. The value of κ close to 1 indicates substantial reduction of modulation. For Hansen's case: only 9% of the original modulation is propagating into the surf zone.

Offshore generation

Other than the previous models, the present section deals with LF wave generation in the region offshore of the breakpoint. Longuet-Higgins and Stewart (1962) argue that the validity of the equilibrium response on a sloping bottom is limited; a steep slope will prevent resonant behavior, and the response will not vary with h^{-2}.

Van Dongeren et al. (2002) presented a parameter which controls the relative importance of surf zone (breakpoint generation) and off-shore forcing. According to Van Dongeren et al. (2002), the linearized shallow water energy equation for the LF waves reads

$$\overline{\frac{\partial F}{\partial x}} + \overline{\frac{Q}{h}\frac{\partial S_{xx}}{\partial x}} = 0, \tag{2.47}$$

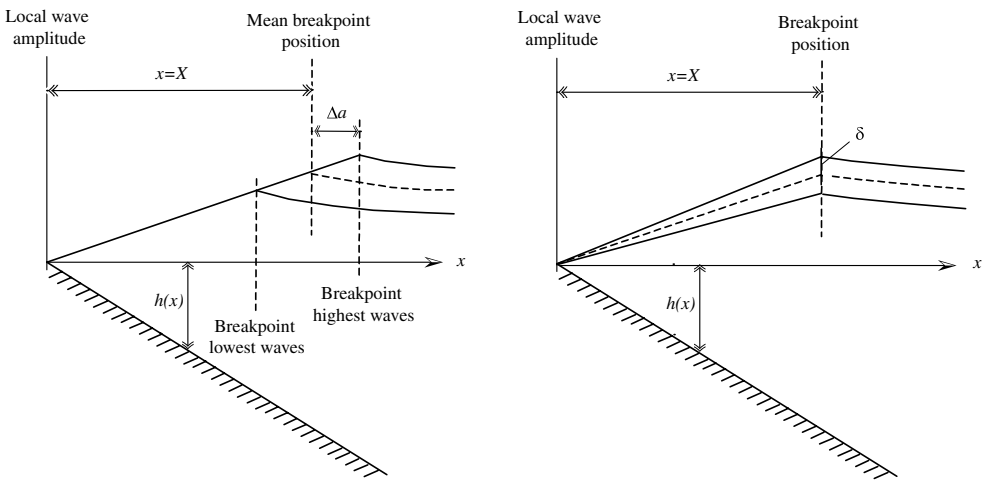


Figure 2.5: Time varying breakpoint (left) and fixed breakpoint (right) characteristics (concepts taken from Schäffer (1993)).

where the second term represents the rate of work that the short waves do on the long waves. Non-dimensionalizing this equation for the shoaling zone and the surf zone using the scales as was presented by Van Dongeren and Svendsen yields for the shoaling zone

$$\overline{\frac{\partial F'}{\partial x'}} + \frac{\Delta\omega}{h_x}\sqrt{\frac{h_s}{g}}\left(1 - \frac{H}{\gamma h_s}\right)\overline{\frac{Q'}{h'}\frac{\partial S'_{xx}}{\partial x'}} = 0, \tag{2.48}$$

and for the surf zone

$$\overline{\frac{\partial F'}{\partial x'}} + \overline{\frac{Q'}{h'}\frac{\partial S'_{xx}}{\partial x'}} = 0, \tag{2.49}$$

where $\Delta\omega$ is the group frequency, h_x the bed slope, h_s the shelf depth, H the wave height and γ the breaking parameter. The parameter in front of the second term in (2.48):

$$\alpha = \frac{\Delta\omega}{h_x}\sqrt{\frac{h_s}{g}}\left(1 - \frac{H}{\gamma h_s}\right), \tag{2.50}$$

controls the size of the term and thus the growth of the energy flux along the slope. The parameter shows some similarity with the χ-parameter proposed by Symonds et al. (1982).
Battjes et al. (2003) showed increasing growth bound wave amplitude varying from $\sim h^{-\frac{1}{4}}$ (Green's Law) to $\sim h^{-\frac{5}{2}}$ for lower and higher frequencies of the subharmonics respectively. A dependency on the normalized bed slope β is proposed, which determines whether or not the slope is 'gentle' or 'steep', observing the growth of the incoming bound wave amplitude.

Chapter 3

Experimental setup

The present chapter describes the previous laboratory experiments concerning long wave generation, the creation of the testprogramme as well as the physical laboratory setup (instrumentation and wave flume) and the procedures used to obtain the measured data.

3.1 Previous work

Kostense (1984) conducted a laboratory study for surf-beat generation on a plane sloping beach ($h_x = 1 : 20$). The testprogramme consisted of bichromatic experiments only. Weakly modulated series ($\delta = 0.2$) were emphasized. Moreover, measurements were taken on the horizontal part of the flume only, disabling the possibility for the observation of bound wave amplitude growth.

Although not focused on long wave generation Boers (1996), but on the sediment transport in the near-shore zone, performed measurements on a barred beach at Delft University of Technology. All test were irregular wave fields since realistic situations had to be simulated. The high spatial resolution of wave gauges made the measurements valuable for studies conducted by e.g. Janssen et al.(2003), Bakkenes (2002) and Battjes et al.(2003).

Baldock et al. (2000) performed 65 bichromatic experiments on a steep, plane beach ($h_x = 1 : 10$). The results show good agreement with the time-varying breakpoint model of Symonds et al. (1982). The observed bound wave frequencies were higher than the lowest primary frequency, which makes the application of the concept of wave groups doubtful. The corresponding values of β for the bichromatic experiments range from 0.13 to 0.8, using 0.4m as the representative depth. The identical physical setup is used for 8 series of experiments with irregular waves. Again, confirmation is found for the time-varying breakpoint model. The amplitude growth is barely analyzed.

3.2 Objectives

Following the objectives of the present thesis (see page 2), more detailed experimental goals are set.

1. Acquire spatial and temporal high resolution data, allowing a quasi-continuous interpretation of the results.

2. Enable comparison of bichromatic results with results originating from irregular wave fields.

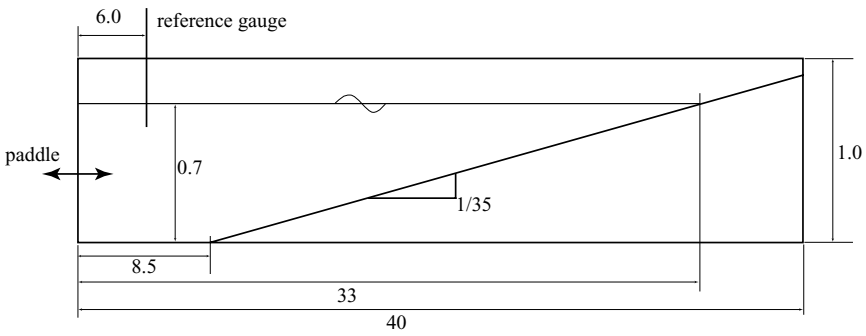


Figure 3.1: Bathymetry and flume dimensions. (All measures in meters)

3. Investigate dependency of the incoming wave amplitude growth on the normalized bed slope β.

3.3 Physical setup

All experiments are performed in the wave flume of the Fluid Mechanics Laboratory at Delft University of Technology. The measurements have been split up into measurements taken on a horizontal bottom and measurements taken on a sloping bathymetry. In order to avoid misunderstanding, these two different situations will be referred to as *cases* exclusively from here on. The horizontal case is introduced for estimation of the incoming wave signal, which is easier compared to the sloping case, since the wave trains propagate with constant speed. In the sloping case, shoaling and phase differences in cross-shore direction (which are actually unknown and therefore subject of this study) hamper the analysis of the wave signal, especially long (low-frequency) components.

Flume and wave generator The bathymetry of the flume in the sloping case is shown in Figure 3.1. The water depth is 0.7m which leaves 0.3m for the crest height, since the flume height is 1.0m. The steepness of the slope $h_x = 1 : 35$ is taken as gentle as possible for a water depth of about 0.7 m. This leaves a long section where waves shoal, but not break. The toe is located 8.5 meters from the wave generator, the first gauge 6.0 m. The horizontal part makes a comparison possible between the sloping and the horizontal case. No gauges are located closer to the wave generator than 6.0 m since the wave generator causes evanescent modes which are assumed to be negligible further than 6.0 m from the wave generator.
The flume has a piston-type wave board. An Active Reflection Compensation (ARC) system absorbs reflected (long) waves. The wave board is capable of generating second-order waves and thus prevents the generation of spurious free waves at that order. The wave board has a maximum stroke of 2m.

3.3.1 Wave gauges

To measure the surface elevation 11 resistance type wave gauges (see Figure 3.4) are used. The gauges measure the conductivity of water by two partially submerged wires. When surface elevation is low, the resistance over the wires is high and vice versa. Since conductivity depends (among others) on the water temperature and presence of dissolved material, calibration of the gauges is performed once a day

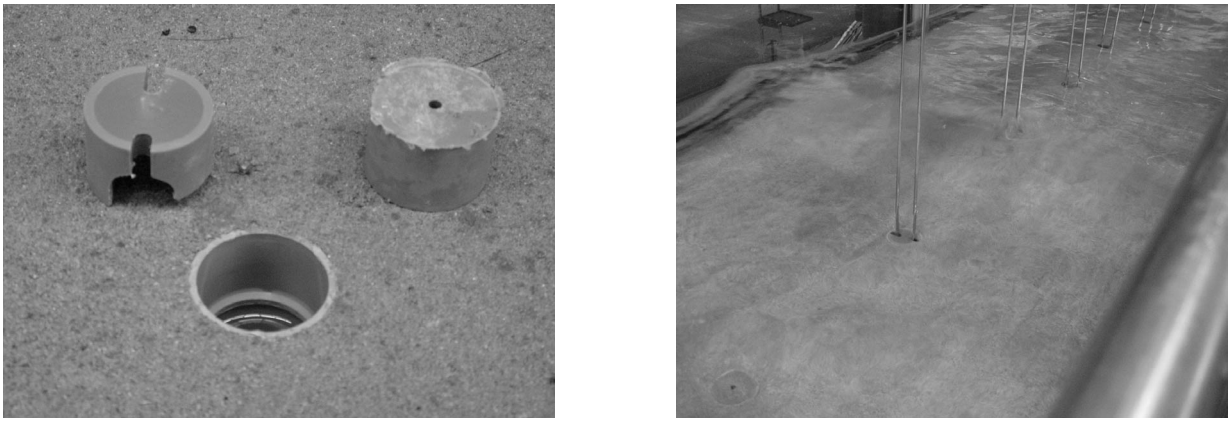


Figure 3.2: Left panel: close up of small hole with lids; left lid is used when a gauge is present, right lid when a gauge is absent Right panel: gauges in shallow water (note small closed hole in bottom left corner).

before the measurements take place. Before calibration, all gauges were cleaned with a little alcohol. The specifications state an accuracy of at least 0.5mm over a range of 0.5m. Because the output varies linearly with the surface elevation, the calibration is simple: all gauges are shifted over exactly 0.3m in height. The corresponding output difference is divided by 0.3m, which leads to a calibration constant in [Volts/meter]. The gauges require a minimum water depth of 5 cm which is not present near the shoreline. Therefore, small diameter, 5 cm deep holes have been made in the slope to guarantee this. A close up of these holes is shown in Figure 3.2. The gauges influence the experiments. In non-breaking waves this disturbance is very little, but in breaking waves they cause air bubbles in the water. The effect of these bubbles on the output of the gauges is unknown. In the analysis the possible effect is ignored and 'breaker-zone' data is dealt with as non-breaking wave data.

The gauge spacing in the horizontal case is optimized for decomposition of wave signals. In order to avoid singularities, the distances between all individual wave gauges are sorted to cover a wide range of wavelengths. The results are shown in Figure 3.3, upper panel. For more details about decomposition and related problems, see Chapter 4. Since wave properties (e.g. amplitude and wavelength) change in the sloping case due to the depth variation, resolution has to be higher than in the horizontal case to obtain a data set which can be treated quasi-continuous. The minimum distance requirement for prevention of electric influence between different gauges is 20 cm is obeyed by using 0.5m between adjacent locations in the non-breaking (shoaling) zone. In the surf zone a smaller value is taken since wave properties change on a smaller spatial scale. The breaker zone spacing is 0.3m. These spacings lead to a number of gauge locations far exceeding the number of available gauges. This is overcome by performing each series a number of times; every such repetition will be referred to as *sessions*, with the gauges at different locations. The data obtained can be combined through the use of a so-called reference gauge, which is located at the same position in all sessions. For more information on the data preparation see section 4.1. To make comparison possible with measurements in the horizontal case, the reference gauge is located in the flat fore-shore in the sloping case. The gauge locations for both cases are shown in Figure 3.3. The point where the gauge distance changes from 0.5 m to 0.3 m is visually determined by the author. The most seaward located depth-induced breakpoint for all series is used for the intermediate distance change and is located at $x = 23$m. The exact locations are shown in Appendix C.

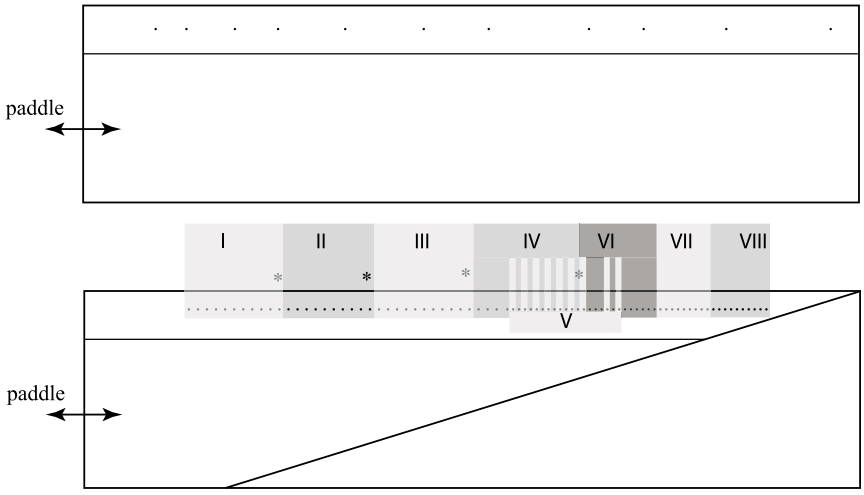


Figure 3.3: Gauge locations. Top panel: horizontal case. Bottom panel: sloping case. The roman numerals denoted the different sessions.

The gauges used for measuring the surface elevation are limited; 11 gauges were available throughout the experiments. Technical specifications of the data acquisition hard- and software prescribe a sampling rate f_s of 25 Hz, which implies a Nyquist frequency $f_N = f_s/2 = 12.5$ Hz, which is sufficient for the observation of short waves.

3.3.2 EMS

At a few locations the particle velocity is measured by an Electro-Magnetic flow meter (E-type) or EMS (see Figure 3.4). This probe measures the velocity in the zx-plane. Its output consists of two signals representing the velocity in x and z direction respectively. Since the output is independent of fluid properties no additional calibration is needed for this probe; the output in Volts can directly be converted into m/s through a known constant, 10 [V/m/s] for the EMS used. Since the working of this probe is based on electro-magnetic resistance of the surrounding water, it should not be used very close to the bottom. A margin of 5 cm is used in the experiments. Combination of velocity information with surface elevation is only possible when both are acquired simultaneous at the same cross-shore position. Since only one EMS is available this velocity information is collected at four positions only. During the session I, II, III an IV the EMS is located at the same location as the most shoreward gauge. Due to the minimum submerged depth of 5 cm needed for proper output, the EMS was only used at the positions shown in Figure 3.3, denoted by the *. Similar to the wave gauges, the sampling rate is 25 Hz. Exact locations of the EMS can be found in Appendix C.

3.3.3 Video

To allow visual observation of the breakpoints of the bichromatic experiments a VHS-video camera is used. The raw video tape is edited and copied on a digital tape, to improve the still-image video quality, which is of great importance in determining breakpoints.

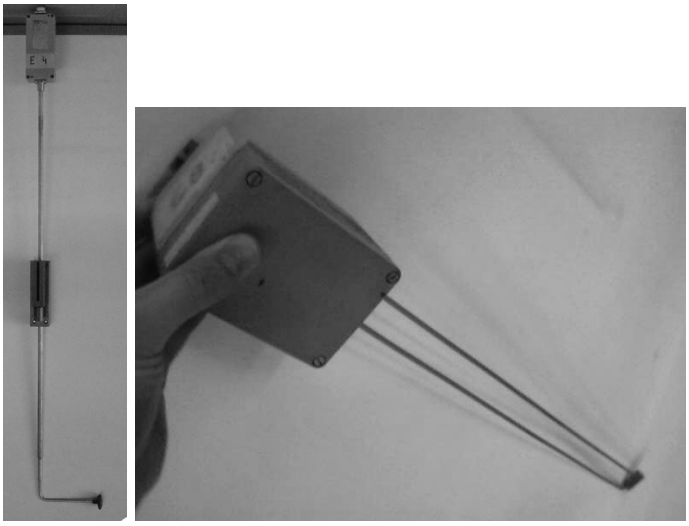


Figure 3.4: EMS (left) and wave gauge (right).

3.3.4 Data-acquisition

All measured data is collected by a PC equipped with a 16 channel data acquisition box and *DasyLab*. The output of the gauge amplifiers is stored directly without any conversion or operation performed. More information on the file coding system, see Appendix C.

3.4 Testprogramme

The testprogramme will consist of two kinds of wave fields; *bichromatic* and *irregular*. The former can be considered as the most basic situation where bound waves occur. The latter represents more realistic wave conditions. Since both wave fields are generated on identical physical setup (depth and bed slope), dependency of amplitude growth on the kind of wave field can be investigated. In the present thesis the bound wave is assumed to behave independently of the wave field. The observations presented by Battjes et al. can therefore be used as a reference in designing the present testprogram. To avoid misunderstanding, the specific wave conditions determined in this chapter will be referred to as *series*.

Duration of the experiments For both irregular and bichromatic experiments a certain equilibrium has to be established after the wave generator has started. Therefore, the length of the recorded time-series is extended with 5 minutes for the bichromatic experiments and 10 minutes for the irregular experiments. The duration of bichromatic experiments is further determined by the sampling rate of the instruments and the accuracy needed in the analysis. The accuracy is expressed in terms of spectral resolution, or the basic frequency f_0, the smallest frequency resolvable in a record of duration T. The relation between these two quantities is shown by

$$f_0 = \frac{1}{T}. \tag{3.1}$$

For the efficient application of the Fast Fourier Transformation (FFT) algorithm, a number of data points equal to an integer power of 2 is needed. Since $N = T * f_s$, this implies

$$T = \frac{2^p}{f_s}, \tag{3.2}$$

which leaves the integer p at our disposal. For $p = 13$ this results in a duration $T = 327.68$ s. This value is used for all bichromatic experiments. For the irregular tests additional requirements are used. In order to get a correct representation of the spectrum, a minimum of thousand (primary) waves is desirable. The total duration of a time record T then becomes $T = 1000T_p$ where T_p is the peak period of the chosen spectrum.

3.4.1 Bichromatic wave experiments

According to the theories discussed in subsection 2.2.3, the generation and release of the bound waves is related to the group frequency. The relevant parameters α and β are dependent of the bound wave frequency as well, as can clearly be seen from (2.42) and (2.50). For this reason the group frequency is varied in the A-series. Observations presented by Battjes et al. (2003) show resonant response near β values of 0.1. For the present setup a representative value for the depth h is taken 0.35m.

The mean frequency $f_{mean} = (f_1 + f_2)/2$ of the primary waves for every A-series is constant for every experiment to avoid variation in the results caused by variation of f_{mean}. The corresponding n-factor[1] for f_{mean}[2] indicates that the primary waves are in the transition zone from deep to shallow water on the horizontal part of the flume.

The deviation of the primary wave frequencies f_1 and f_2 from this mean value determines the bound wave frequency $f_b = f_1 - f_2$. The spectra of the bichromatic experiments must be narrow banded (see Appendix A). For this reason the lowest primary frequency is at least twice the bound wave frequency f_b in all series.

The relative importance between offshore forcing and breakpoint forcing is expressed by the α-parameter value. A higher value expects the offshore forcing to be more important. Since the energy transfer is subject of the present study, a varying α parameter should lead to varying growth behavior. The group frequency of series A-5 is small compared to the other series and accounts for breakpoint generated waves, which are expected to observed considering the value of α being smaller than 1.

The B-series account for a variation in amplitude. Higher amplitudes imply earlier breaking, which is expected to lead to smaller total enhancement of the forced waves. Since the steepness H/L probably plays a role in the LW-generation process, the modulation is varied in the B-series. If the generation process is amplitude dependent, there should be some kind of correlation between the modulation and the amplitude of the generated long wave. The exact determination of the primary wave frequencies, for both A and B-series, is based using multiples of f_0 (see previous section). This is shown in Table 3.2. The cut-off value between high frequencies and low frequencies is taken $81f_0$.

Considering the values shown in Table 3.2, it can be seen that every value is even, which means that the duration of the time record T, is allowed to become half the value of 327.68s, due to whatever reason, without causing spectral leakage. (For more information on spectral leakage, see Appendix B.)

[1] $n = 0.74$

[2] $f_{mean} = 0.57$

series	a_1 [m]	a_2 [m]	δ [-]	f_1 [Hz]	f_2 [Hz]	f_b [Hz]	α [-]	χ [-]	β [-]	$(H/L)_\infty$ [-]
A-1	0.06	0.012	0.2	0.6714	0.4761	0.1953	6.5563	28.209	0.123	0.030
A-2	0.06	0.012	0.2	0.6470	0.5005	0.1465	4.9172	15.867	0.164	0.030
A-3	0.06	0.012	0.2	0.6348	0.5127	0.1221	4.0977	11.019	0.197	0.030
A-4	0.06	0.012	0.2	0.6226	0.5249	0.0977	3.2781	7.052	0.246	0.030
A-5	0.06	0.012	0.2	0.5859	0.5615	0.0244	0.8195	0.440	0.987	0.030
B-1	0.06	0.012	0.2	0.6470	0.5005	0.1465	4.9172	15.867	0.164	0.030
B-2	0.06	0.018	0.3	0.6470	0.5005	0.1465	4.9172	15.867	0.164	0.033
B-3	0.06	0.024	0.4	0.6470	0.5005	0.1465	4.9172	15.867	0.164	0.035
B-4	0.06	0.03	0.5	0.6470	0.5005	0.1465	4.9172	15.867	0.164	0.038
B-5	0.06	0.036	0.6	0.6470	0.5005	0.1465	4.9172	15.867	0.164	0.040

Table 3.1: Parameters of bichromatic experiments

series	f_1	f_2	f_{mean}	f_g
A-1	220	156	188	64
A-2	212	164	188	48
A-3	208	168	188	40
A-4	204	172	188	32
A-5	192	184	188	8

Table 3.2: Frequencies of bichromatic series in terms of multiples of the basic frequency f_0.

series	f_p [Hz]	T_p [s]	H_{m0} [m]	Duration [min]
C-1	0.50	2.00	0.050	40
C-2	0.50	2.00	0.075	40
C-3	0.50	2.00	0.100	40
D-1	0.65	1.54	0.050	31
D-2	0.65	1.54	0.075	31
D-3	0.65	1.54	0.100	31

Table 3.3: Wave parameters, series C and D.

3.4.2 Irregular wave experiments

For the irregular test the Jonswap spectrum shape is chosen for its narrowbandedness and the fact that it is a realistic (observed) spectrum. More or less similar to the design of the bichromatic programme, the amplitude (represented by H_{m0}) and the frequency (represented by the peak frequency f_p) are varied. Although the wave field is irregular, the generation of the irregular waves is deterministic, which allows the series to be split up in the previously defined sessions.

Chapter 4

Data analysis

The present chapter discusses the techniques used to translate the raw data into information making interpretation (see Chapter 5) possible. First of all, the raw data files are converted to Matlab files (`*.mat`) and checked for errors. The checked results are combined into one single file and is decomposed into several different wave components. The separation procedure is tested before application to laboratory data.

4.1 Data preparation

After each session, the measured data was subjected to three tests to detect errors in the physical setup and in the wave signal. First, the presence of a signal was examined[1]. Second, the output value of the gauge amplifiers was inspected. Due to the limited range of the wave gauges, the waves can exceed these limits if the gauge is not properly installed. Thus if exceeding occurs, the recorded signal would then show a constant value equal to 10 Volts or -10 Volts. The third test calculates the variance density of the signal[2]. If gauges were calibrated inaccurately, the variance density would deviate considerably from the variance densities originating from other gauges.
A more qualitative verification of the data is performed by plotting the amplitude spectra of all gauging locations in one 3-D plot (see Figure 4.1). The plots should show smooth lines for constant frequencies. Similar plots for all experiments can be found in Appendix C on page 53. Detailed information on the data preparation can be found in Appendix C as well.

4.1.1 Composition of simultaneous time series

The required spatial resolution was determined in subsection 3.3.1. Every session was performed using a reference gauge at $x = 6$m. The data recorded by this gauge is synchronous to the data recorded by the other gauges in the same session. To compose a data set as if 80 gauges were used simultaneously, the time difference between the 8 reference gauge signals is calculated by using the cross-correlation function

[1] `value_check.m`
[2] `gauge_check???.m` The question marks are wildcards for the different series names (e.g. A-1).

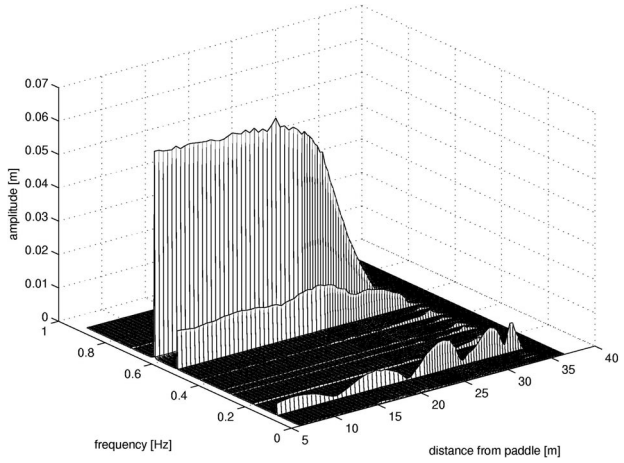


Figure 4.1: Amplitude spectra for series A-4.

R_{xy} of the reference gauge data.

$$R_{xy}(m) = E\{X(t)Y(t+m)\} \qquad \text{with} \qquad E\{X\} = 0 \qquad \text{and} \qquad E\{Y\} = 0, \tag{4.1}$$

where m is the timelag at which the correlation is calculated and $X(t)$ and $X(t)$ denote the time series of the reference gauge recorded in two distinct sessions. The timelag with the largest corresponding value of R_{xy} is the time difference between the reference gauge signals. Since the reference gauges signal recorded synchronous with the signals of the gauges in the same session, synchronization of the 8 reference gauge signals implies synchronization of the other wave signals as well.
The maximum time lag is found to be ± 20 seconds. The result of this shift is shown in Figure 4.3. This figure also shows the accurate wave reproduction of the generator.

4.1.2 Wave reproduction

The reproduction accuracy is checked by comparison of two wave signals by cross-correlating them. The wave signals are recorded in the horizontal case. The wave generator is operated identically for the two measurements and the locations of the gauges are not changed. This should yield a cross-covariance factor near 1. Differences in reproduction yield deviations from 1 especially for the longer (irregular wave) time series. Results are shown in Figure 4.2. This accurate reproduction allows us to use 1 gauge located at a fixed position along the flume as a reference gauge as described in the previous section.
The horizontal case enables the separation of the wave signal in three components without the problems that would arise when a slope is present. The separation of the signal into three components gives us information about the accuracy of the ARC.
The ARC equipped wave generator should absorb any free outgoing waves, in other words no incoming free waves should be detected by the gauges. Deviations from this ideal case can be caused by the following possibilities:

- ARC does not absorb 100% of the outgoing wave,
- the generation of the second order incoming bound wave is not perfect and causes spurious waves,

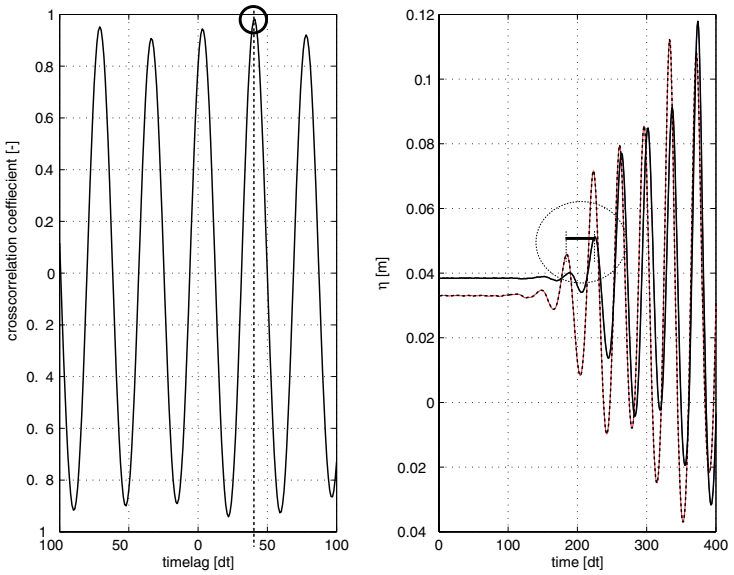


Figure 4.2: Reproduction of wave signal for series A-1. Left panel: cross-variance with maximum value at timelag value of $42 \cdot dt$. Right panel: Corresponding correlated time series with time shift of $42 \cdot dt$.

- measuring noise in the gauge locations causes noise in the output of the method,
- the primary waves do not behave according to linear theory.

4.2 Decomposition

4.2.1 General

Reflection of waves due to the limited length of the wave flume affects the wave signal recorded by the wave gauges. Several separation or decomposition techniques are available some of which will be discussed in this chapter as well as the applied technique in the present analysis. To avoid misunderstanding, from here on, waves travelling shoreward will be referred to as *incoming* waves. Waves travelling in the opposite direction, seaward, will be referred to as *outgoing* waves.

Thornton and Calhoun (1972) and Goda and Suzuki (1976) presented decomposition methods based on two-point measurements of wave gauges and pressure sensors. These two-point methods have a limited frequency range: the spacing between the two gauges determines the coherence factor which determines the relative phase stability for every frequency component. This stability decreases with increasing frequency, in other words: the distance between the gauges cannot be large compared to the wavelength. A second limitation is the critical gauge spacing: if the gauge spacing is equal to $x = nL/2$ with $n = 0, 1, 2, \ldots$, the system of equations is singular. For near-singular spacing the results are not reliable. More physically, the two gauges cannot "see" whether the wave is an incoming or an outgoing wave (see Figure 4.4). To avoid this problem, Mansard and Funke (1980) used a least squares approach in the case of three wave gauges. Zelt and Skjelbreia (1992) presented a weighing technique for an arbitrary number of gauges which makes

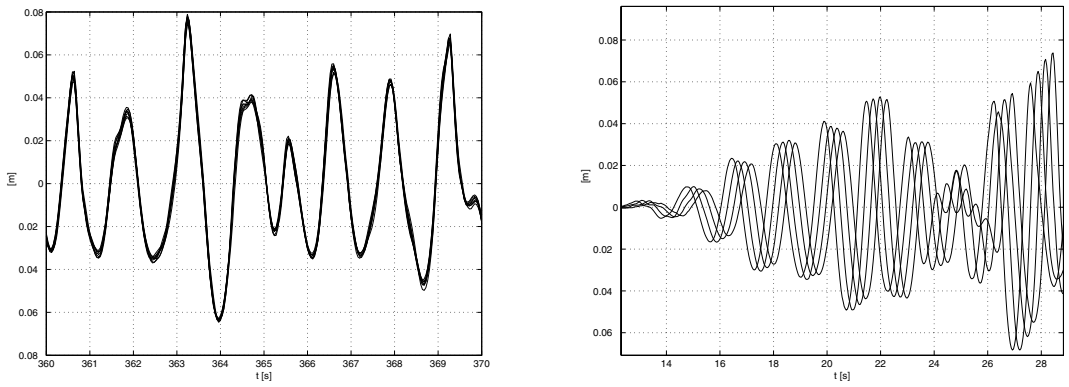


Figure 4.3: Shifted reference gauge time series for D-3 experiments. Left panel: wave records of the reference gauge for 4 distinct sessions. Right panel: wave records of 4 adjacent gauge locations from distinct sessions.

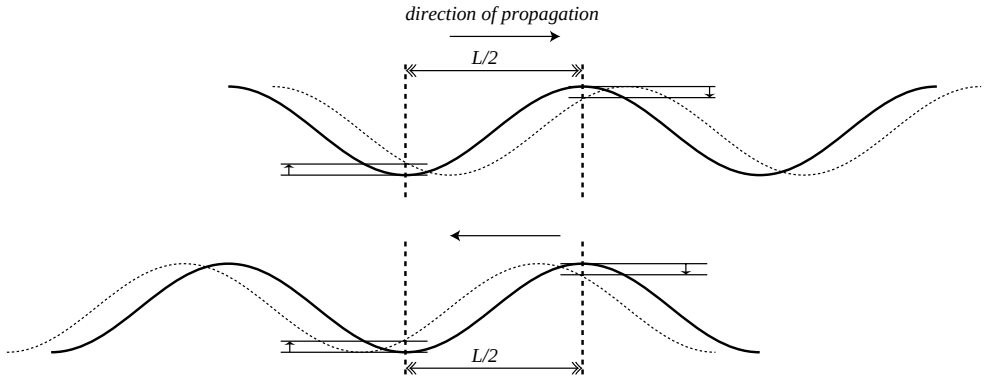


Figure 4.4: Critical gauge spacing; waves propagating in different directions can not be separated using two gauges (dashed lines) only. The change in surface elevation detected by the wave gauges is similar for both wave directions.

near-singularity values less important. All discussed methods above are based on linear wave theory and applicable for free waves, they are not applicable for bound waves since these waves do not comply with the (linear) dispersion relationship. Bakkenes (2002) presents a decomposition method for bound waves. Although this method did not result in reliable output when used on a slope, this method is used in the horizontal case for accurate estimation of the generated (incoming) wave signal and will be discussed in the following section.

4.2.2 Horizontal case

Analysis of the "horizontal" data will make clear how to deal with the incoming free wave signal. We define that if the amplitude of this component is larger than 5% of the outgoing free wave amplitude, it cannot be neglected in the analysis of the sloping case.
The surface elevation $\eta(x_p, t)$ is recorded at a series of locations $\{x_p\}$, $p = 1, 2, \ldots, D$ as shown in Figure 4.5.

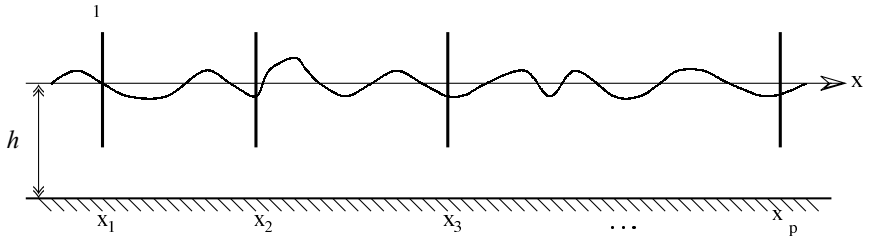


Figure 4.5: Measurement setup.

Using Fourier analysis we can express the surface elevation $\eta(x_p, t)$

$$\eta(x_p, t) = \sum_{j=0}^{N-1} A_{j,p} e^{i\omega_j t}, \tag{4.2}$$

where $\omega_j = 2\pi j/T$, $A_{j,p}$ represents the complex amplitude of the jth frequency component, T is the length of the time series and N the number of samples in T, related by the sampling rate f_s; $N = f_s T$. For incoming free waves (propagating in positive x-direction on a horizontal bottom) the phase difference between $x = 0$ and $x = x_p$, $\Phi_{j,p}$ obeys

$$\Phi_{j,p} = -k_j x_p. \tag{4.3}$$

The wavenumber k_j is calculated from the linear dispersion relation (2.9) for frequency ω_j.
Since the decomposition method for LF waves differs from the method used to decompose HF waves, the analyses for HF and LF waves are discussed separately in the following two subsections.

High frequency waves

The lower limit of the HF range is determined by the width of the (free) wave amplitude spectrum. In this thesis $81 \cdot f_0$ is used as cut-off value. This value is applicable for the analysis of irregular waves as well. The upper limit is equal to half the sampling rate, known as the Nyquist frequency f_N. For this frequency range we assume the surface elevation $\eta(x_p, t)$ to be the sum of two components, incoming and outgoing free waves, expressed by the following Fourier sum

$$\eta(x_p, t) = \sum_{j=82}^{N/2-1} \left\{ \frac{(a_{in,j} e^{i\Phi_{j,p}} + a_{out,j} e^{-i\Phi_{j,p}})}{2} \right\} e^{i\omega_j t} + *, \tag{4.4}$$

where the $*$ denotes the complex conjugated of the preceding term, $\omega_j = j\omega_1$ with $\omega_1 = 2\pi f_0$, $a_{in,j}$ and $a_{out,j}$ are complex values representing amplitude and phase for incoming and outgoing waves respectively for frequency ω_j for $x = 0$. Combination of (4.2) and (4.4) yields for the HF range

$$A_{j,p} = a_{in,j} e^{i\Phi_{j,p}} + a_{out,j} e^{-i\Phi_{j,p}} \qquad \text{with} \qquad p = 1, 2, \ldots, P+1. \tag{4.5}$$

If only two gauges are available, the above equation can be solved exactly. For $P > 1$ the system is over-determined and a least squares method is used to calculate $a_{in,j}$ and $a_{out,j}$[3]. For the calculation all

[3] `decomp.m`

available gauge data are used ($P = 11$). Written in matrix notation

$$\begin{bmatrix} e^{i\Phi_{j,1}} & e^{-i\Phi_{j,1}} \\ e^{i\Phi_{j,2}} & e^{-i\Phi_{j,2}} \\ \vdots & \vdots \\ e^{i\Phi_{j,P}} & e^{-i\Phi_{j,P}} \end{bmatrix} \begin{bmatrix} a_{in,j} \\ a_{out,j} \end{bmatrix} = \begin{bmatrix} A_{j,1} \\ A_{j,2} \\ \vdots \\ A_{j,P} \end{bmatrix}. \tag{4.6}$$

Results for the separation are shown in Figure 4.6. Results for all experiments are shown in Appendix C. The incident HF amplitude values are used to calculate the incident bound wave amplitude[4] ζ_t following the equilibrium theory presented by Longuet-Higgins and Stewart (1962). In Table 4.2 ζ_t can be compared with the results of the LF separation, presented in the following subsection.

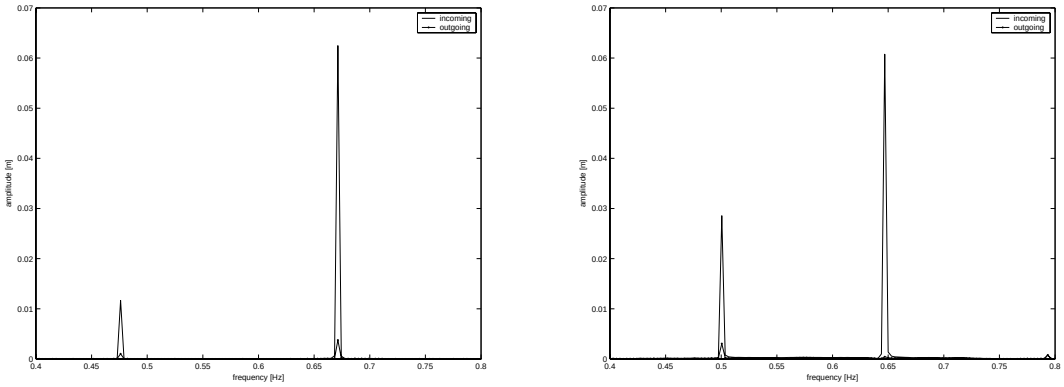


Figure 4.6: Amplitude spectra for incoming and outgoing free HF waves. Left panel: series A-1. Right panel: series B-4.

Low frequency waves

For the low frequency motion the system of equations (4.6) is extended with an incoming bound component. The surface elevation η is expressed as

$$\eta(x_p, t) = \sum_{j=1}^{81} \left\{ \frac{(a_{in,j} e^{i\Phi_{j,p}} + a_{out,j} e^{-i\Phi_{j,p}} + a_{bo,j} e^{i\Phi_{bo,j,p}})}{2} \right\} e^{i\omega_j t} + *, \tag{4.7}$$

where $a_{bo,j}$ represents the complex amplitude of the bound wave with frequency ω_j. The phase difference is calculated from the wave number of the bound wave k_{bo}, which is a result of the primary waves (see Figure 2.3):

$$k_{bo} = \frac{\Delta\omega}{c_{g,f_{mean}}}. \tag{4.8}$$

The phase Φ_{bo} for incoming bound waves on a horizontal bathymetry then obeys

$$\Phi_{bo} = -k_{bo} x, \tag{4.9}$$

[4] `bichrotriton.m`

	input [m]	output [m]
incoming free amplitude	0.0002	0.00020000316918
outgoing free amplitude	0.0010	0.00100000182295
incoming bound amplitude	0.0020	0.00200000052600

Table 4.1: Results of decomposition of wave signal.

and in matrix notation the LF separation can be written

$$\begin{bmatrix} e^{i\Phi_{j,1}} & e^{-i\Phi_{j,1}} & e^{i\Phi_{bo,j,1}} \\ e^{i\Phi_{j,2}} & e^{-i\Phi_{j,2}} & e^{i\Phi_{bo,j,2}} \\ \vdots & \vdots & \vdots \\ e^{i\Phi_{j,P}} & e^{-i\Phi_{j,P}} & e^{i\Phi_{bo,j,P}} \end{bmatrix} \begin{bmatrix} a_{in,j} \\ a_{out,j} \\ a_{bo,j} \end{bmatrix} = \begin{bmatrix} A_{j,1} \\ A_{j,2} \\ \vdots \\ A_{j,P} \end{bmatrix}. \tag{4.10}$$

This separation procedure is tested using a signal[5] with known properties (see Equation 4.2.2). Since the amplitudes of the three components are known, the results of the above procedure can be verified. Results of this comparison are shown in Equation 4.2.2. The results are in excellent agreement with the input values. In other words; waves behaving according to the assumptions made in the decomposition method — no energy loss and known phase behavior — are very well separated.
Results of the LF separation of laboratory data are shown in Table 4.2. The observed reflection $R = a_{in}/a_{out}$ can be compared with the reflection values of the wave generator (see Figure 4.7) provided by the manufacturer. The observed values range from 0.158 to 0.2812, in contrast to the manufacturer's values ranging from 0.01 to 0.03 for the bound wave frequencies. It is noted that the incoming free wave amplitude lies within the accuracy of the wave gauges. The possible causes mentioned before (see page 23) may account for the deviation between observed and manufacturer's values. Because the latter two possible reasons are hard to quantify, the incoming free wave is assumed to be fully caused by inappropriate wave generation (the first two). It is now assumed that the wave generator generates identical deviations for each session. This enables the separated incoming free wave signal to be translated, using linear theory, and subtracted from the wave signal in the sloping case. The remaining signal then consists of two components; incoming bound waves and outgoing free waves. This will be dealt with in the following section.

4.2.3 Sloping case

Prior to decomposition, the estimated incoming free wave component is subtracted from the signal. Since this component is a free wave, the amplitude and phase information $a_{in,j}$, as a result of the decomposition[6] in the horizontal case, is used to make time signals for every gauge location[7]. Based on the assumptions that the wave generator generates identical waves every session, the time series used for decomposition on the horizontal bottom are synchronous to the time series in the sloping case. The estimated incoming free bound wave amplitude based on measurements on horizontal bottom are converted to time series for every

[5] `synth2.m`
[6] `decompH3.m`
[7] `incomingfree.m`

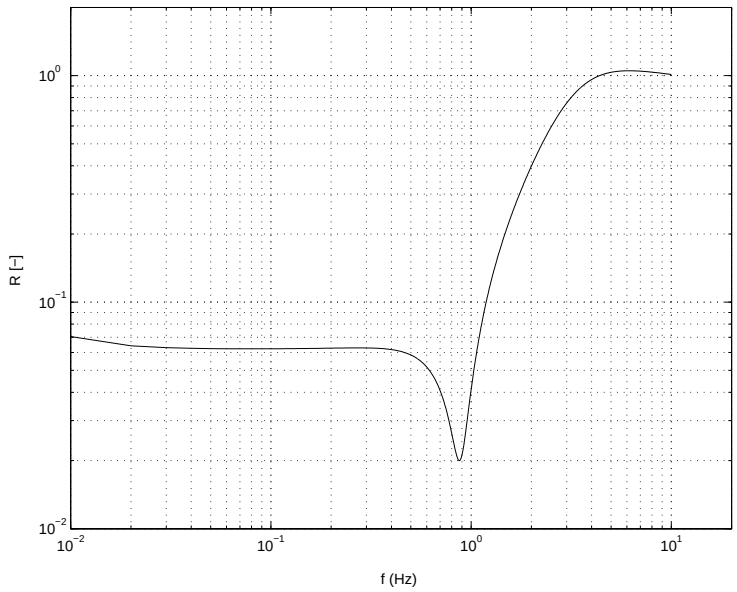


Figure 4.7: Reflection coefficients for the used wave generator.

gauge location using linear shoaling, and free wave phase difference $\Phi_{j,p}$, calculated from

$$\Phi_{j,p} = -\int_0^{x_p} k_j(x)dx, \tag{4.11}$$

since the wavenumber k is dependent on the local water depth. The resulting time series can be subtracted from the time series obtained in the horizontal case as they were synchronous. The bound wave phase difference $\Phi_{bo,j,p}$ is calculated from

$$\Phi_{bo,j,p} = -\int_0^{x_p} \frac{\omega_j}{c_{g,f_{mean}}}dx \tag{4.12}$$

where $c_{g,f_{mean}}$ is the group speed for the mean primary frequency f_{mean}. Since the shoaling of the incoming bound wave is unknown, as well as the exact behavior of the outgoing free wave, an attempt is made to develop a method to resolving the shoaling properties without knowing them *a priori*. This is done by means of iteration using the *array* method. Wave records of $P+1$ gauges, the array, or window, are used to obtain estimations for the incoming and outgoing LF waves.

4.2.4 First calculation

Similar to the method presented by Bakkenes (2002), in the first calculation step, the amplitude of the incoming bound wave and is assumed to be constant over a gauge array. For the outgoing wave this is assumed as well in contrast to Bakkenes's method, which uses Green's Law for the outgoing free wave. Since the outgoing LF free wave is likely to exchange energy with the incoming wave groups (see e.g. observations presented by Battjes et al. (2003)) Green's law may be a good estimation for the observed *trend*. For calculation over a gauge array, especially in the region(s) where the outgoing wave amplitude increases when moving seaward, Green's Law would deviate qualitatively from the amplitude behavior.

	HF				LF			
	target values		measurements		bound waves		free waves	
series	a_1 [m]	a_2 [m]	$a_{1,inc}$ [m]	$a_{2,inc}$ [m]	ζ_t [m]	$a_{in,bo}$ [m]	a_{in} [mm]	a_{out} [m]
A-1	0.06	0.012	0.0625	0.008	0.0016	0.0017	0.1919	0.0012
A-2	0.06	0.012	0.0609	0.008	0.0016	0.0016	0.2435	0.0011
A-3	0.06	0.012	0.0606	0.008	0.0016	0.0015	0.2804	0.0010
A-4	0.06	0.012	0.0601	0.009	0.0016	0.0015	0.1890	0.0010
A-5	0.06	0.012	0.0600	0.023	0.0016	0.0015	0.3176	0.0012
B-1	0.06	0.012	0.0609	0.008	0.0016	0.0016	0.2435	0.0011
B-2	0.06	0.018	0.0611	0.012	0.0024	0.0024	0.3698	0.0016
B-3	0.06	0.024	0.0610	0.016	0.0033	0.0032	0.4998	0.0020
B-4	0.06	0.030	0.0608	0.020	0.0041	0.0039	0.5847	0.0025
B-5	0.06	0.036	0.0603	0.024	0.0049	0.0047	0.7034	0.0029

Table 4.2: Amplitude target values and measured values for primary and bound components.

Therefore no amplitude growth is assumed (K=1). In matrix notation the above can be written for an array consisting of $P+1$ (adjacent) gauges as

$$\begin{bmatrix} e^{-i\Phi_{j,p-P/2}} & e^{i\Phi_{bo,j,p-P/2}} \\ \vdots & \vdots \\ e^{-i\Phi_{j,p-1}} & e^{i\Phi_{bo,j,p-1}} \\ e^{-i\Phi_{j,p}} & e^{i\Phi_{bo,j,p}} \\ e^{-i\Phi_{j,p+1}} & e^{i\Phi_{bo,j,p+1}} \\ \vdots & \vdots \\ e^{-i\Phi_{j,q+P/2}} & e^{i\Phi_{bo,j,p+P/2}} \end{bmatrix} \begin{bmatrix} a^{(1)}_{out,j,0,p} \\ a^{(1)}_{bo,j,0,p} \end{bmatrix} = \begin{bmatrix} A_{j,p-P/2} \\ \vdots \\ A_{j,p-1} \\ A_{j,p} \\ A_{j,p+1} \\ \vdots \\ A_{j,p+P/2}. \end{bmatrix}. \tag{4.13}$$

or

$$\mathbf{B_{p,P,j}a^{(1)}_{j,0}} = \mathbf{A_{j,p,P}} \tag{4.14}$$

where P is a positive even integer. The phase-matrix $B_{p,P,j}$ is based on phase differences between x_p and $x = 0$m. The estimated $a_{out,j,0,p}$ and $a_{bo,j,0,p}$ are thus estimations for $x = 0$. These values are translated to the amplitudes on the slope by evaluating

$$a^{(1)}_{bo,j,p} = a^{(1)}_{bo,j,0,p} e^{i\Phi_{bo,j,p}} \quad \text{and} \quad a^{(1)}_{out,j,p} = a^{(1)}_{out,j,0,p} e^{-i\Phi_{j,p}} \tag{4.15}$$

For inspection of the accuracy of the separation, an artificial signal is made with known shoaling behavior. The incoming bound wave amplitude grows with (an arbitrarily) chosen proportionality: $\propto h^{-1}$. The outgoing wave amplitude is modulated[8]. This can be expected in the experiments, considering the results of e.g. Van Dongeren (1997) and Battjes et al. (2003). Since the available 67 gauge locations enable only $67 - P$ different array locations, $67 - P$ estimations remain after the first calculation. The results of the separation are shown in Figure 4.8 for array lengths of 3 and 5 gauges.

[8] according $1 + 0.15x \sin(0.8x)$.

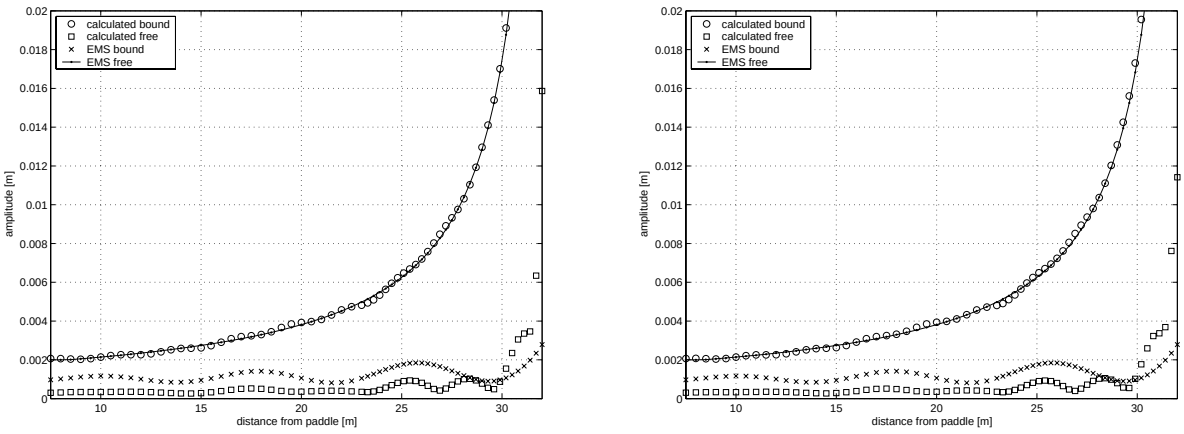


Figure 4.8: Test results of decomposition, sloping case, step one. Left panel: 3-gauge array, right panel: 5-gauge array.

The estimation of the incoming bound wave is surprisingly good. The outgoing free wave, however, deviates substantially from its expected value. Especially in the region where the artificial incoming bound wave amplitude is very large, the deviation of the outgoing free wave is substantial.

4.2.5 Second calculation

The bound wave growth (probably) deviates more from the assumed non-shoaling behavior in the first step. The implementation of the (accurate) results of the first step should yield a improved estimation for both the incoming and outgoing LF waves. The (real) bound wave shoaling factors for the bound wave can be expressed

$$K^{(2)}_{bo,j,p} = \frac{|a_{bo,j,p}|^{(1)}}{|a_{bo,j,1+P/2}|^{(1)}} \tag{4.16}$$

These shoaling factors $K^{(2)}_{bo,j,p}$ are used in a second calculation according

$$\begin{bmatrix} e^{-i\Phi_{j,p-P/2}} & K^{(2)}_{bo,j,p-P/2}e^{i\Phi_{bo,j,p-P/2}} \\ \vdots & \vdots \\ e^{-i\Phi_{j,p-1}} & K^{(2)}_{bo,j,p-1}e^{i\Phi_{bo,j,p-1}} \\ e^{-i\Phi_{j,p}} & K^{(2)}_{bo,j,p}e^{i\Phi_{bo,j,p}} \\ e^{-i\Phi_{j,p+1}} & K^{(2)}_{bo,j,p+1}e^{i\Phi_{bo,j,p+1}} \\ \vdots & \vdots \\ e^{-i\Phi_{j,p+P/2}} & K^{(2)}_{bo,j,p+P/2}e^{i\Phi_{bo,j,p+P/2}} \end{bmatrix} \begin{bmatrix} a^{(2)}_{out,j,0,p} \\ a^{(2)}_{bo,j,0,p} \end{bmatrix} = \begin{bmatrix} A_{j,p-P/2} \\ \vdots \\ A_{j,p-1} \\ A_{j,p} \\ A_{j,p+1} \vdots \\ A_{j,p+P/2} \end{bmatrix}. \tag{4.17}$$

and the estimations for each location p

$$a^{(2)}_{out,j,p} = a^{(2)}_{out,j,0,p}e^{-i\Phi_{j,p}} \qquad \text{and} \qquad a_{bo,j,0,p}e^{i}\Phi_{bo,j,p} \tag{4.18}$$

Phase-wise this separation is identical to (4.13). The difference lies in the (real) amplitude part of the $P \times 2$-matrix entries. Similar to the first step, the free wave amplitude is now expected to be constant

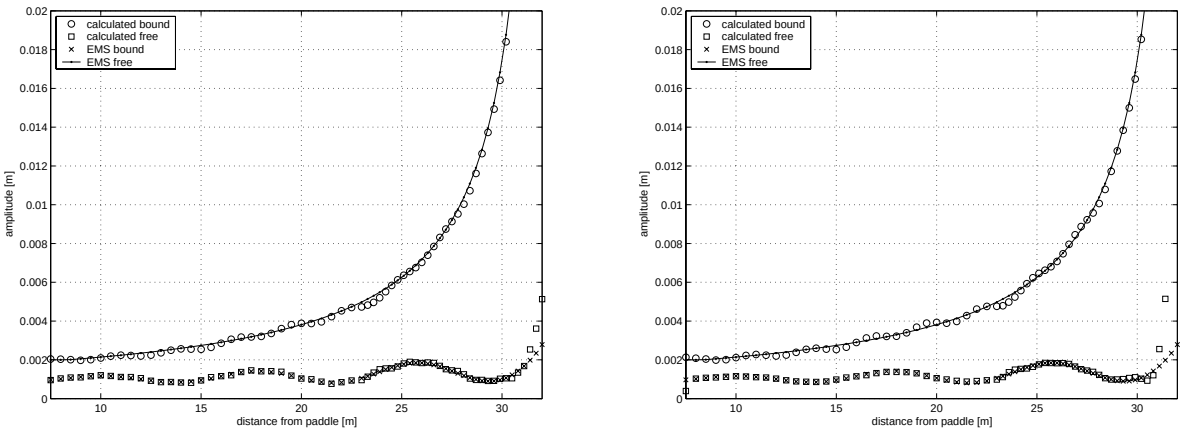


Figure 4.9: Test results of decomposition, sloping case, step two. Left panel: 3-gauge array, right panel: 5-gauge array.

over an array. The bound wave amplitude is now expected to shoal over an array, using the results of the first step. The results of the second step are shown in Figure 4.9. Again, a 3-gauge and 5-gauge array are used for the analysis. It can be seen from Figure 4.9 that the bound wave amplitude estimation, slightly deteriorates in the second calculation.

4.2.6 Third calculation

The last step in the iteration process combines the results of the previous two. For the bound wave shoaling (4.16) is used, the outgoing free wave shoaling behavior is implemented in a way similar to the bound wave implementation in the second step. We write for the shoaling factors

$$K^{(3)}_{out,j,p} = \frac{|a^{(2)}_{out,j,p}|}{|a_{out,j,P+1}|} \qquad \text{and} \qquad K^{(3)}_{bo,j,p} = K^{(2)}_{bo,j,p} \tag{4.19}$$

this yields in matrix notation

$$\begin{bmatrix} K^{(3)}_{out,j,p-P/2}e^{-i\Phi_{j,p-P/2}} & K^{(2)}_{bo,j,p-P/2}e^{i\Phi_{bo,j,p-P/2}} \\ \vdots & \vdots \\ K^{(3)}_{out,j,p-1}e^{-i\Phi_{j,p-1}} & K^{(2)}_{bo,j,p-1}e^{i\Phi_{bo,j,p-1}} \\ K^{(3)}_{out,j,p}e^{-i\Phi_{j,p}} & K^{(2)}_{bo,j,p}e^{i\Phi_{bo,j,p}} \\ K^{(3)}_{out,j,p+1}e^{-i\Phi_{j,p+1}} & K^{(2)}_{bo,j,p+1}e^{i\Phi_{bo,j,p+1}} \\ \vdots & \vdots \\ K^{(3)}_{out,j,p+P/2}e^{-i\Phi_{j,p+P/2}} & K^{(2)}_{bo,j,p+P/2}e^{i\Phi_{bo,j,p+P/2}} \end{bmatrix} \begin{bmatrix} a^{(3)}_{out,j,0,p} \\ a^{(3)}_{bo,j,0,p} \end{bmatrix} = \begin{bmatrix} A_{j,p-P/2} \\ \vdots \\ A_{j,p-1} \\ A_{j,p} \\ A_{j,p+1} \vdots \\ A_{j,p+P/2}. \end{bmatrix}. \tag{4.20}$$

and similar to the previous steps, the estimations for $x = 0$ are transformed for $x = x_p$ by evaluating

$$a^{(3)}_{bo,j,p} = a^{(3)}_{bo,j,0,p}e^{i\Phi_{bo,j,p}} \qquad \text{and} \qquad a^{(3)}_{out,j,p} = a^{(3)}_{out,j,0,p}e^{-i\Phi_{j,p}} \tag{4.21}$$

Results of the third iteration are shown in Figure 4.10. More iteration steps can be performed at the cost of reliable data points this Since the decomposition method estimates bound and free wave amplitudes at the

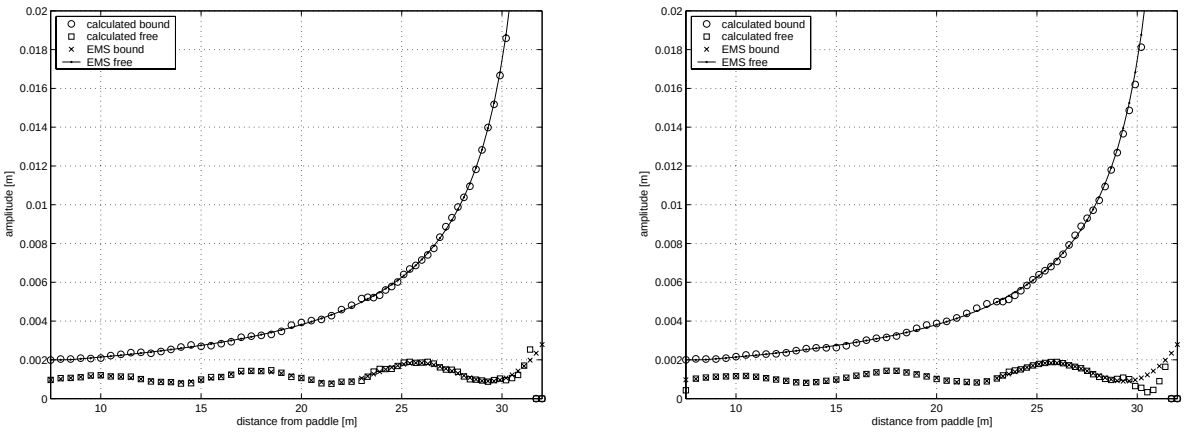


Figure 4.10: Test results of decomposition, sloping case, step three. Left panel: 3-gauge array, right panel: 5-gauge array.

middle gauge of a gauge array, the first and last $P/2$ gauging locations are not well-estimated when using $P+1$ gauges in an array. Therefore each iteration step decreases the number of reliable gauge locations. However, more gauges increase the accuracy of the results in terms of suppressing measuring noise. The assumptions that no shoaling occurs over a gauge array makes large gauge lengths inaccurate. Therefore, as a result of this trade-off, an array of 5 adjacent gauges (equivalent to $P = 4$) is used for the estimation of the amplitudes at the middle gauge. From the 81 available gauging locations, the analysis is performed on the gauges 'seaward' of the still-water shoreline. These 67 locations yield, with the approach of (4.10) or (4.13) over a 5-gauge window, 63 estimations of $a^{(1)}_{bo,j,p}$ and $a^{(1)}_{out,j,p}$ after the first iteration. To check the sensitivity of the iteration method for incoming free wave signals the clean signal is accommodated with a, small amplitude, incoming free wave (about 15% of the outgoing wave amplitude). The separation then results in the estimations shown in Figure 4.11. The deviations of these results differ only little from the results obtained with a noiseless signal. The incoming free wave eventuates in a slight underestimation of the bound wave amplitude estimation, which can be seen in the region 10 - 17m from the wave generator. The outgoing wave amplitude seems unaffected by the added incoming component.

4.3 EMS data

The velocity data recorded by the EMS is used for validating the decomposition method. The LF surface elevation ζ_j is assumed to be a superposition of incoming ($\zeta_{bo,j}$) and outgoing ($\zeta_{out,j}$) waves. For the discharge Q a similar assumption is adopted (for $Q_{bo,j}$ $Q_{out,j}$), as in Van Dongeren (1997). Then, assuming that the waves propagate without change of shape, the discharge is related to the LF surface elevation by

$$Q_{bo,j} = c_g \zeta_{bo,j} \qquad \text{and} \qquad Q_{out,j} = -\sqrt{gh}\zeta_{out,j}, \tag{4.22}$$

where c_g represents the group speed of the primary waves. With the above assumptions we may solve for $\zeta_{bo,j}$ and $\zeta_{out,j}$

$$\zeta_{bo,j} = \frac{\zeta_j \sqrt{gh} + Q_{bo,j}}{c_g + \sqrt{gh}} \qquad \text{and} \qquad \zeta_{out,j} = \frac{\zeta_j c_g - Q_{out,j}}{c_g + \sqrt{gh}} \tag{4.23}$$

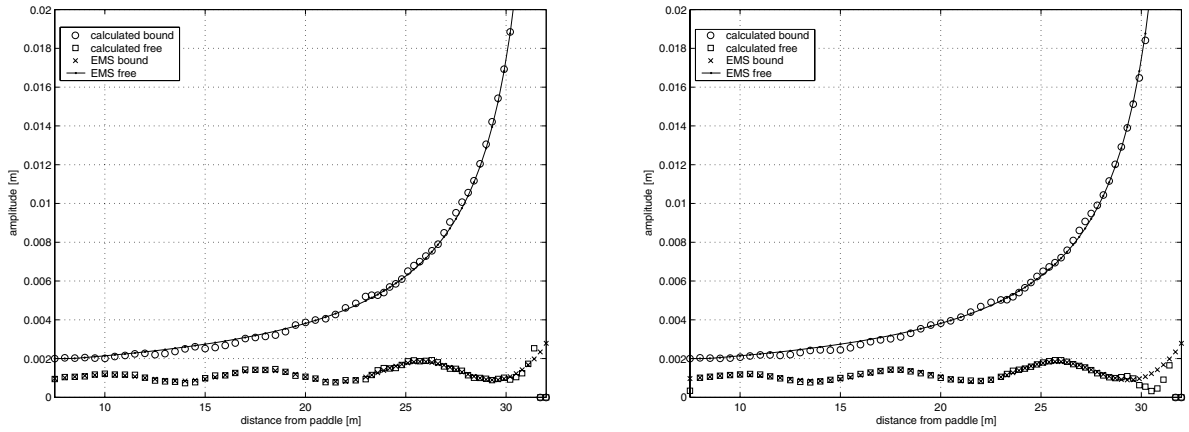


Figure 4.11: Test results of decomposition with polluted signal, iteration step two. Left panel: 3-gauge array, right panel: 5-gauge array.

as derived in Van Dongeren (1997). For shallow water $c_g \approx \sqrt{gh}$, and reduces (4.23) to

$$\zeta_{bo,j} = \frac{\zeta_j + u\sqrt{h/g}}{2} \qquad \text{and} \qquad \zeta_{out,j} = \frac{\zeta_j - u\sqrt{h/g}}{2} \tag{4.24}$$

where u is the horizontal particle velocity originating from the EMS measurements and the relation with the discharge is given by $u = Q/h$. The above method was presented by Guza et al. (1984). The amplitude of ζ_{bo} and ζ_{out} can be derived by applying the Hilbert transformation.
The results are plotted in Figure 4.12, because only one EMS-gauge is available, and a co-located gauge is necessary, only four locations are provided with this additional information. The agreement with the array method is discussed in the following chapter.

4.4 Phaselagging

The energy transfer model is based on a phase lag between incoming HF envelope and the incoming and outgoing LF motion. The present measurements are therefore analyzed to observe the phase relations between HF and LF waves. The envelope $W(x_p, t)$ is determined for each location using Hilbert transformation. Fourier analysis for the bound wave frequency ω_j yields the complex amplitude $w_{j,p}$ of the squared HF envelope at $x = x_p$

$$w_{j,p} = W(x_p, t)^2 e^{i\omega_j t}. \tag{4.25}$$

The total phase difference ψ is calculated from

$$\psi_{j,p} = \arg\left(\frac{V_{j,p}}{a_{bo,j}}\right). \tag{4.26}$$

The additional phase lag away from π can be calculated as

$$\Delta\psi_{j,p} = \psi_{j,p} - \pi. \tag{4.27}$$

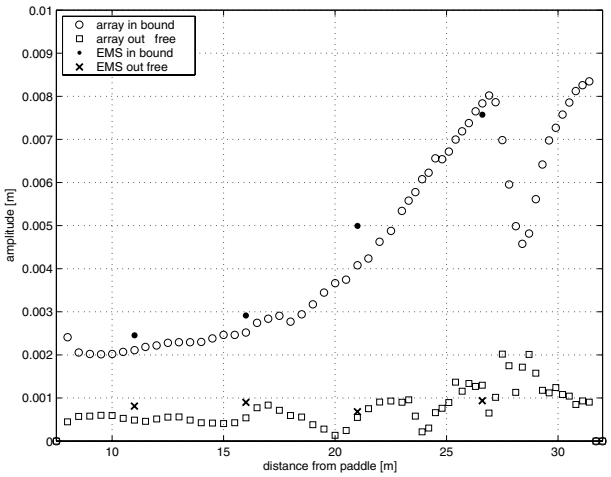


Figure 4.12: Results of EMS decomposition, sloping case, series A-1 (circles and crosses) and results from the array method using a 5-gauge window.

According to the energy transfer model, a value of $\Delta\Psi_{j,p} \neq n\pi$, with $n \in \mathbb{N}$, enables work to be done by the HF waves on the LF waves.
The amount of energy is calculated by the forcing term in the long wave energy equation. The spatial change in flux F balances the work done on the LF waves. For the incoming LF wave we write

$$\frac{\partial \overline{F}}{\partial x} + \overline{\frac{Q_{bo,j}}{h}\frac{\partial S_{xx}}{\partial x}} = 0. \tag{4.28}$$

In the shoaling zone, the second term can be rewritten

$$R \equiv \left\langle u\frac{\mathrm{d}S_{xx}}{\mathrm{d}x}\right\rangle \cong \frac{1}{2}\kappa\hat{U}\hat{S}\sin(\Delta\psi) \qquad \text{with} \qquad u = \frac{Q}{h}, \tag{4.29}$$

where κ is the LF wavenumber, $\hat{S}$ represents the amplitude of S_{xx} and $\hat{U}$ the amplitude of the horizontal, long wave, particle velocity U.

$$\hat{U}_{bo,j} = (c_g\hat{\zeta}_{bo,j})/h, \tag{4.30}$$

where c_g is the group speed of the primary waves. For the outgoing wave. A similar approach can be adopted for the energy transfer from the short wave groups and the outgoing wave; $a_{bo,j}$ in (4.26) is then replaced by $a_{out,j}$ and $\zeta_{bo,j}$ can be replaced by $\zeta_{out,j}$. Plots for phase lag, work and amplitudes are shown in Figure 4.13 for both incoming and outgoing LF waves. As the outgoing free wave propagates in opposite direction of the HF waves, the phase difference between these component grows faster than the phase difference between the incoming HF wave envelope and the incoming LF motion. Moreover, it can be seen from Figure 4.13 that the maximum phase lag of the envelope and incoming LF wave is smaller than π. The amplitude is therefore expected to grow throughout the shoaling zone. The outgoing wave phase difference with the envelope covers the whole range from $-\pi$ to π. Therefore, as a result of the rapidly changing energy transfer the amplitude of the outgoing wave will increase and decrease at specific points along the flume. The amplitude, work and phase lag evolution in cross-shore direction for series B-2 are shown in Figure 4.13 and in Appendix D.

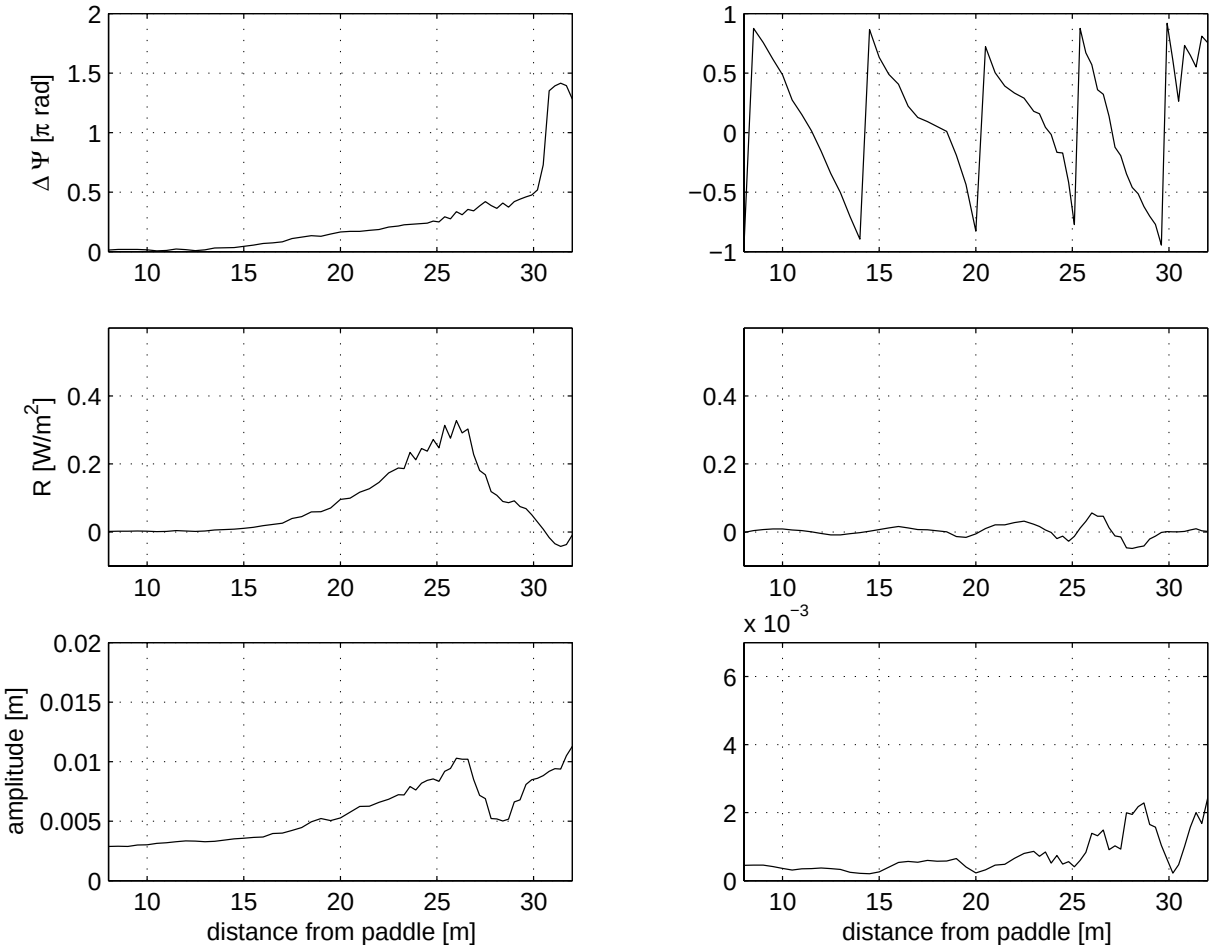


Figure 4.13: Phase lag $\Delta\Psi$, work R and amplitudes of series B-2. Top row: phase lag. Middle row: work done by HF waves of LF waves. Bottom row: amplitude. Left column: incoming waves. Right column: outgoing waves. Similar plots for other series can be found in Appendix D.

Chapter 5

Analysis results

The present chapter discusses the results of the analysis of the bichromatic experiments. The observations for incoming and outgoing waves are compared to computed results based on the energy transfer model presented in chapter 4. Finally, the testprogramme and observations are evaluated.

5.1 Incoming waves

5.1.1 Observations

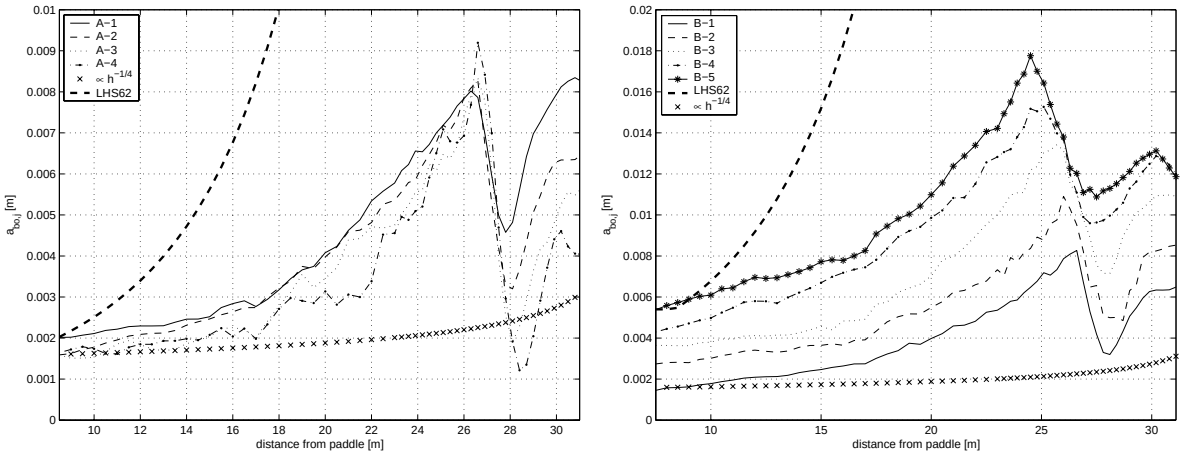


Figure 5.1: Amplitudes of incoming LF waves: series A (left) and series B (right). The upper and lower boundaries are based on an incoming amplitude of on the highest and lowest amplitude respectively at $x = 7.5$m.

Amplitude The spatial evolution of the incoming amplitude for series A and B is plotted in Figure 5.1. The upper and lower boundaries, given by the equilibrium response and Green's law respectively are plotted as well. The A-5[1] graph is lower than the lower boundary for $14 \leq x \leq 19$m and at $24 \leq x \leq 25$m.

[1]Due to the long LF wave length of the A-5 series, an array length of 11 gauges is used. Fewer estimations are therefore available for this series.

Series A-1 shows a larger initial amplitude (amplitude at $x = 6$m). Apart from these exceptions, the A and B series are between the upper and lower boundaries in the zone seaward of the breaker zone. The abnormality of A-5 in this respect can be a result of the iteration method. Comparison of EMS estimations with the results of the first iteration from the array method shows fairly good agreement. A decrease of the (incoming) amplitude near $x = 16$m is observed after the first step and is amplified in the second step. Moreover, the EMS-estimations show no values lower than the $h^{-1/4}$ line at all. The amplitude growth based on EMS-estimations only, fits in the observed general trend for A-2, A-3 and A-4; lower frequencies show weaker amplitude growth. Series A-1 shows almost identical growth as A-2 despite its larger initial amplitude. For the reason of the observed abnormality A-5 is left out of consideration in the following chapters.

The maximum amplitude is roughly equal for series A-1 through A-4. The location where this occurs is equal as well and coincides with the point where the lowest waves break ($x = 26.7$m). Moving shoreward, the amplitude decreases rapidly to a local minimum value. This value shows large variation for the different series A, indicating frequency dependent behavior in the surf zone. Series B (having equal group frequencies) agrees with this; approximately the same value is found at $x = 28$ (see Figure 5.2).

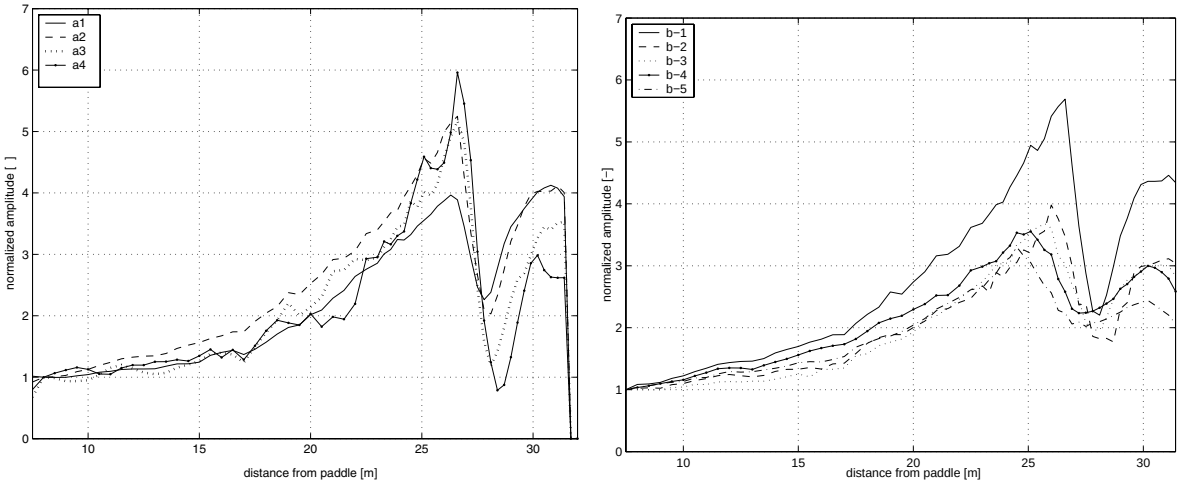


Figure 5.2: Normalized amplitudes: series A (left) and series B (right). Normalization was performed with the amplitude estimation at $x = 7.5$m

From Figure 5.1 and Figure 5.2 showing the observed and normalized amplitudes of incoming LF waves for series a and b, it can be seen that shoreward of $x \approx 17$m, amplitudes of series A-1, A-2, A-3 and A-4 (although oscillating), tend to increase faster than seaward of this location. From the point of initial breaking to the shoreline, the amplitude response increases with increasing LW frequency. Series A-3 and A-4 show oscillatory behavior.

The modulation varying B-series show an increase of initial amplitude with increasing modulation, which is expected, since larger modulation implies a larger spatial gradient of radiation stress and thus larger bound wave amplitudes (see Figure 5.1). The location where the largest amplitude for each B-series is found, moves seaward with increasing modulation. Similar to the A-series, the amplitude rapidly decreases to a local minimum value in the breaker zone. For the B-series, this value is still larger than energy conservative shoaling would yield (see Figure 5.1). From the normalized amplitudes for series B, series B-1 deviates considerably from the other B-series. This is unexpected since the β values are equal for all

B-series.

Phase For the A and B-series it is clear that the observed growth is larger than conservative shoaling (see Figure 5.1). The phase lag between the HF wave envelope and the LF waves is expected to enable the energy transfer. The observed phase lags between incoming HF envelope and incoming LF motion are shown in Figure 5.3. For all A and B-series, except series A-5, the phase lag increases continuously when travelling shoreward. A phase lag larger than $\pi/2$ is not reached seaward of the breaker zone.

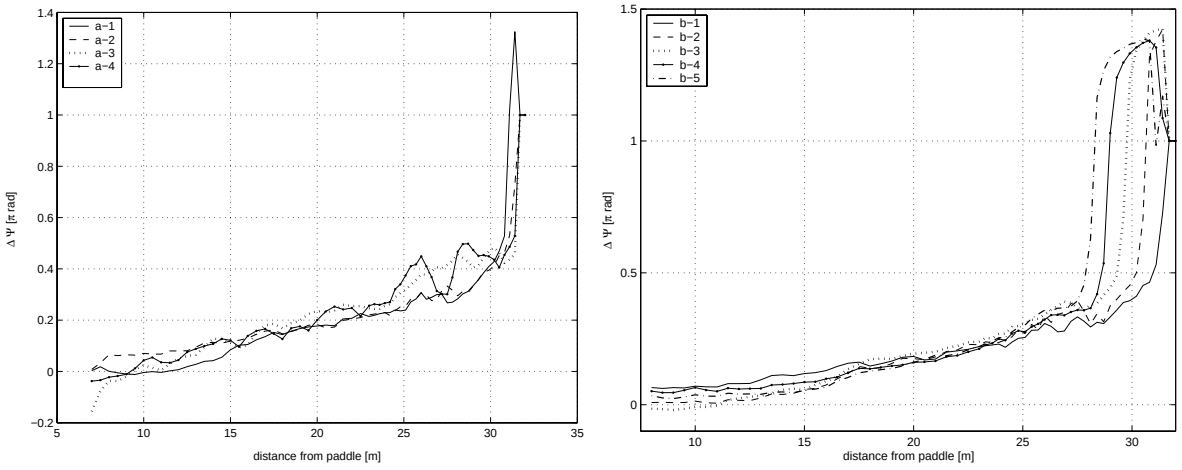


Figure 5.3: Phase differences between incoming short wave envelope and incoming bound long wave: series A (left) and series B (right).

The B-series phase lag shows a large jump in the surf zone, which can be the result of inverted groupiness as was mentioned in subsection 2.2.3. The location of the observed phase jump moves seaward for increasing modulation. The phase difference in the region prior to breaking is quite similar for all B-series. The graph of series B-1 shows less steepness than other B-series, but the deviation is small. No peculiar phase behavior is observed near $x = 17$m despite the aforementioned change in amplitude growth at that location for both A and B-series.

5.1.2 Model comparison

The *observed* amplitude growth is compared with the *expected* growth based on the energy transfer model. Based on the observed phase lag $\Delta\Psi$ (see (4.27)), the work done on the long waves R (see (4.29)) is calculated and shown in Figure 5.4.

From Figure 5.4 it can be seen that the steepness of the lines, increases near $x = 17$m for series B-3, B-4 and B-5. This is in agreement with the observation of higher amplitude growth shoreward of $x \approx 17$m.

If the energy conserving model (4.29) holds, integration of the energy balance yields an estimation for the LF energy flux, from hereon called the *computed* LF energy flux, F^*. The latter is compared to the *observed* energy flux, F, based on the incoming LF amplitude. The comparison will clarify to what extent

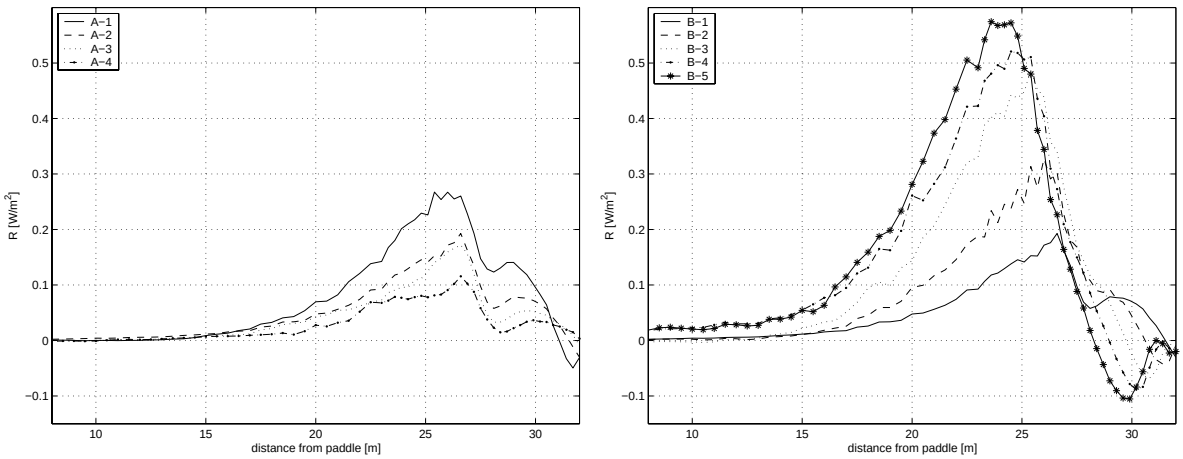


Figure 5.4: Work done on incoming LF waves: series A (left) and series B (right).

the energy transfer model is correct. Amplitudes values are obtained from the energy flux F^*, through

$$a^*_{bo} = \sqrt{\frac{2F^*}{\rho g c_g}}. \tag{5.1}$$

Here c_g is the group speed of the primary waves and a^*_{bo} is the computed amplitude corresponding to F^*. The values of a^*_{bo} and a_{bo} are shown in Figure 5.5 for series A-1 and A-2. The behavior of B-2 is representative for the other B-series.

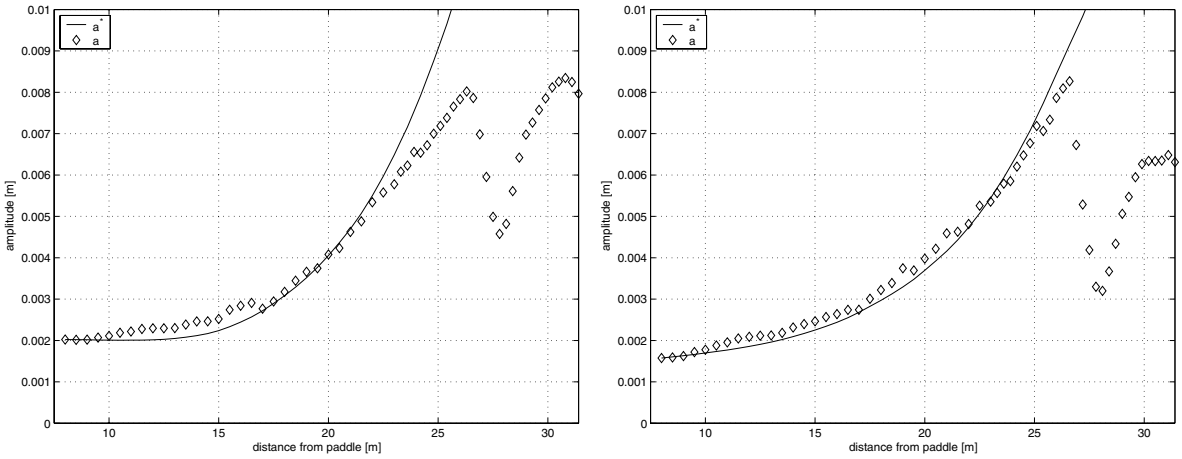


Figure 5.5: Incoming LF amplitudes. Observed amplitude a_{bo} ($\diamond$) and computed amplitude a^*_{bo} (solid line) for series A-1 (left) and series A-2 (equal to B-1) (right).

The agreement between the observed and the computed values is quite good in the region where $x < 20$m for series A-1. Shoreward of this region, the observed flux F is increasingly smaller than the energy conserved flux F^*. Series A-2 shows similar deviation near the breaker zone, although less pronounced. This indicates increasing importance of energy dissipation for higher LW frequencies.

5.2 Outgoing waves

5.2.1 Observations

Amplitude Seaward of the breaker zone all series show oscillations around a mean value, which through visual comparison seems well approximated by Green's Law, indicating net energy conservation for the outgoing wave. In the breaker zone, the outgoing amplitude changes rapidly. Both increasing (A-2, A-4 and A-5) and decreasing (A-3) behavior is observed. The amplitude seaward of the breaker zone is distinctively larger for the A-3 and A-4 series. For the A-4 series the amplitude of the outgoing wave is larger than the incoming wave amplitude.

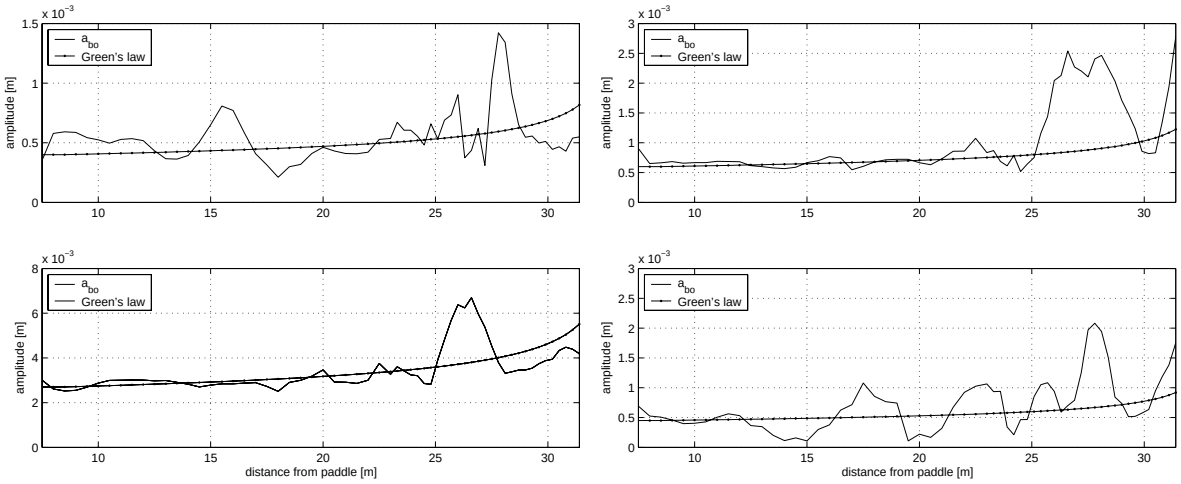


Figure 5.6: Outgoing LF wave amplitude, series A-1 (top left), A-4 (bottom left), B-1 (top right) and B-3 (bottom right).

All B-series show outgoing wave amplitudes with roughly the same value, although the incoming wave amplitudes vary from 1.7mm to 5.5mm. The outgoing wave generation (or reflection) seems independent for incoming wave amplitudes. (see Figure 5.7) Since the (mean) outgoing wave amplitude hardly varies. Near $x = 20$m all B-series show small amplitudes, indicating energy transfer to the HF waves. Since the B-series have identical bound wave frequencies, energy transfer to HF waves will occur at identical locations.

Phase The outgoing waves show a rapid increase of phase difference with respect to the incoming wave envelope. From Figure 5.8 it can be seen for the A-series that higher LW frequencies show a larger rate of increase, which is logical, since higher frequencies have higher wave numbers. The B-series show an stepwise behavior. The steepness of the graphs decreases for higher modulations.

5.2.2 Model comparison

Similar to the procedure used for the incoming waves, the observed energy flux F is compared to the computed flux F^*. In Figure 5.9, it is clear that large differences exist between both fluxes. It is noted that some agreement can be found in the locations of (local) maximum or minimum values.

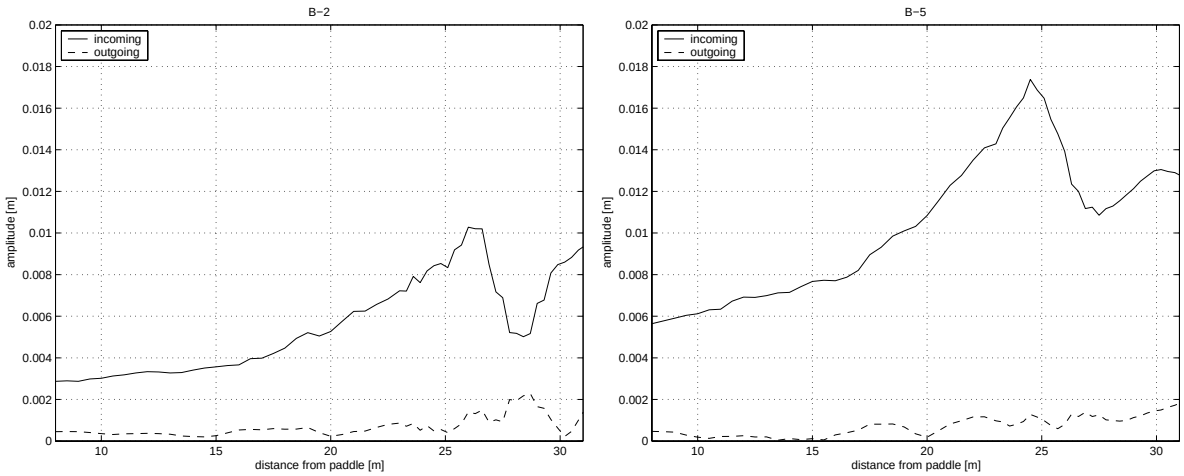


Figure 5.7: Incoming and outgoing amplitudes for series B-2 (left) and B-5 (right). Similar plots for remaining series can be found in Appendix D.

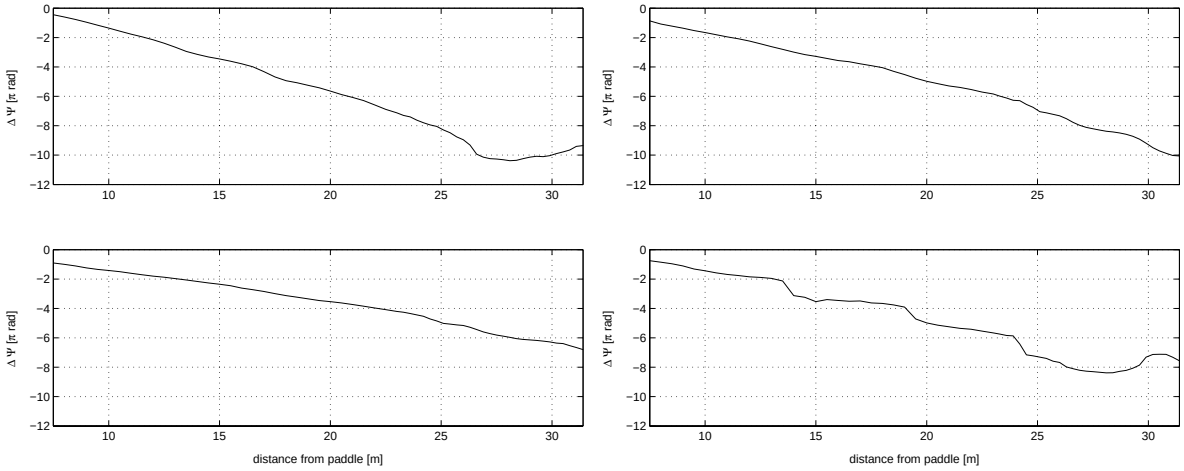


Figure 5.8: Phase difference between incoming short wave envelope and outgoing LF waves for series A-1 (top left), A-3 (bottom left), B-1 (top right) and B-3 (bottom right)

5.3 Evaluation of testprogramme

The variation of β was expected to be related to the enhancement of the bound long wave amplitude. Based on the energy conservation model, the observed work done on the LF waves is now used for amplitude behavior prediction. For series A-1 through A-4, computed values are shown in Figure 5.10. This figure clearly shows larger growth for higher LW frequencies, which was expected considering Battjes et al. (2003).

Since the amplitude estimations a^*_{bo} are based on measured quantities, it is not fair to compare the growth of a^*_{bo} with the equilibrium growth rates in shallow water $\propto h^{-5/2}$, since this proportionality is based on energy conservation of the HF waves. Considering the energy flux of the HF waves, it is clear that dissipation is

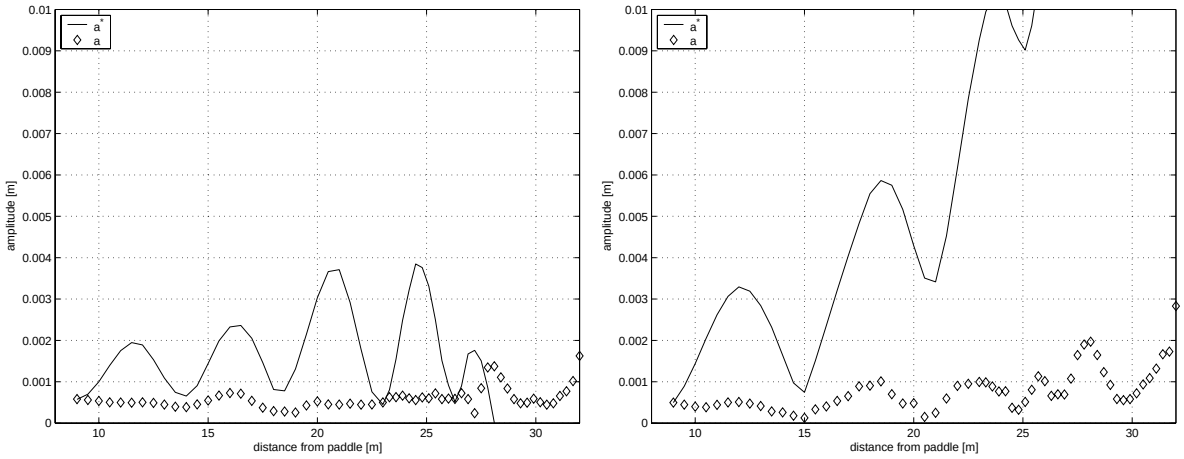


Figure 5.9: Computed outgoing LF amplitude a^* and observed outgoing amplitude a for series A-1(left) and B-3 (right)

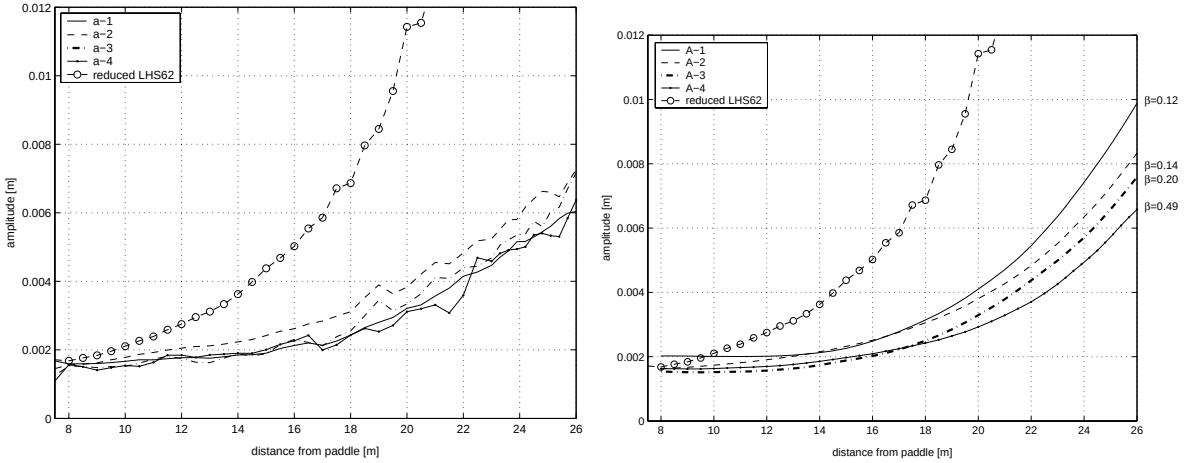


Figure 5.10: Observed incoming bound wave amplitudes (left) and computed amplitudes (right). Reduced LHS62 represents the equilibrium amplitude with the observed HF amplitudes.

not negligible as the incoming HF amplitude does not increase when travelling shoreward, while growth proportional to $h^{-1/4}$ is expected. In Figure 5.10 the observed bound wave amplitudes are therefore compared to the 'reduced' equilibrium amplitude using *observed* HF wave amplitudes. Comparison of $a^*_{bo,j}$ to the 'reduced' equilibrium amplitude growth yields the conclusion that for the present wave conditions and setup, the equilibrium response is impossible, since the HF waves dissipate substantial energy when moving shoreward.

Moreover, the LF waves still grow much slower than the 'reduced' equilibrium response. This is in correspondence with the suggestions made by Battjes et al. (2003) concerning the values of β, which is 0.12 in the A-1 series and increasing to 0.49 for the A-4 series.

Although near-resonant response is not observed from the very start of the flume, but near $x = 17$m, an increase in amplitude growth is observed. The β-value for this location is for series A-2 is 0.14, indicating

a transition for the given wave conditions from gentle to steep.

With respect to α variation (see section 3.4) and (2.50), the following is said. Series A-5 was intended to lead to a domination of breakpoint generated waves, but the analysis results were doubtful. No conclusions are therefore drawn concerning α.

The expectations of the enhancement of the amplitude with varying modulations, thus steepness, are confirmed by Figure 5.2. The breaking process starts further offshore for higher wave amplitudes (occurring at higher modulations) and the energy transfer is terminated there. In other words: lower modulated waves lead to larger enhancement of the incoming bound wave.

Chapter 6

Conclusions and Recommendations

6.1 Conclusions

From the present experiments, analysis and results, the following conclusions are drawn:

- A high resolution data set is obtained, making extensive study for long wave generation possible. The set consists of nine bichromatic and six irregular tests each with 81 wave gauge locations including the swash zone.
- The decomposition technique presented by Bakkenes (2002) is extended with two iterative steps which leads to more accurate estimations of incoming and outgoing wave amplitudes.
- A energy conserving model transferring energy from HF waves to LF waves is compared to the present observations; good agreement was found for the incoming LF wave amplitude growth and the work done on the LF waves. The outgoing wave barely shows agreement.
- Based on the observed LF energy flux, offshore generation is mildly frequency dependent and agrees qualitatively (higher β values show less growth) and quantitatively (increasing growth was observed at locations with β values of approximately 0.14) with the β characterization as presented by Battjes et al. (2003).
- The reflection of the present bed slope depends on the incoming bound wave frequency. For certain values the reflected wave amplitude is larger than the incoming wave amplitude. This is especially interesting in situations where equilibrium growth coincides with requirements for high reflection.

6.2 Recommendations

- Additional laboratory tests are recommended to be carried out, with β values smaller than 0.1.
- Research of the outgoing wave amplitude and phase behavior, correspondence was not found between the observations and the model results in the present thesis.
- Equivalent analysis of the irregular wave data and comparison with the present results. In the comparison with the results of Battjes et al. and the present results, it is assumed that LF wave motion acts independent of the of wave field type (bichromatic or irregular).

- Analysis of recordings in the swash zone. Similar to observations done by Battjes et al. (2003), large energy losses occur in the swash zone under certain wave conditions. Since the present data set comprises recordings in the swash zone, analysis can reveal the relevant processes causing the energy loss.
- Numerical modelling using the present setup and test programme. If the present results agree with numerical simulations, experiments can be performed with a wide variety of varying parameters, e.g. bed slope and water depth.

Bibliography

Bakkenes, H. J. (2002). Observation and separation of bound and free low-frequency waves in the nearshore zone. Master's thesis, Delft University of Technology.

Baldock, T. E. and D. A. Huntley (2002). Long wave forcing by the breaking of random gravity waves on a beach. In *Proc. Roy. Soc. Lond. A*, pp. 2177–2201.

Baldock, T. E., D. A. Huntley, P. A. D. Bird, T. O'Hare, and G. N. Bullock (2000). Breakpoint generated surf beat induced by bichromatic wave groups. *Coastal Engineering 39*(39), 213–242.

Battjes, J. A. (2001). *Korte Golven*. Delft University of Technology. lecture notes.

Battjes, J. A., H. J. Bakkenes, T. T. Janssen, and A. R. van Dongeren (2003). Shoaling of forced infragravity waves. submitted to JGR.

Biésel, F. (1952). Équations génénerales au second ordre de houle irrégulière. *La Houille Blanche*, 372–376.

Boers, M. (1996). Simulation of surf zone with a barred beach; report 1: Wave heights and wave breaking. communications.

Dean, R. G. and R. A. Dalrymple (1984). *Water wave mechanics for engineers and scientists*. New Jersey: Prentice Hall, Englewood Cliffs.

Goda, Y. and Y. Suzuki (1976). Estimation of incident and reflected waves in random wave experiments. In *Proc. 15th Coastal Engineering Conference*, Hawaii, pp. 828–845.

Guza, R. T., E. B. Thornton, and R. A. Holman (1984). Swash on steep and shallow beaches. *Proc.of the* 19^{th} *International Conference on Coastal Engineering ASCE 1*, 708–723.

Hansen, J. B. (1990). Periodic waves in the surf zone: analysis of experimental data. *Coastal Engineering 14*, 19–41.

Janssen, T. T., J. A. Battjes, and A. R. van Dongeren (2003). Long waves induced by short-wave groups over a sloping bottom. accepted for publication in JGR.

Kostense, J. K. (1984). Measurements of surf beat and set-down beneath wave groups. In *Proc. 19th Int. Conf. Coastal Eng.*, pp. 724–740.

Longuet-Higgins, M. S. and R. W. Stewart (1962). Radiation stress and mass transport in gravity waves with application to 'surf beats'. *J. Fluid Mech. 13*, 481–504.

Mansard, E. P. D. and E. R. Funke (1980). The measurement of incident and reflected spectra using a least squares method. In *Proc. 17th Int. Conf. Coastal Eng.*, New York, pp. 154–172.

Munk, W. H. (1949). Surf beats. *Trans. Am. Geoph. Union 30*, 849–854.

Schäffer, H. A. (1993). Infragravity waves induced by short-wave groups. *Journal of Fluid Mechanics 247*, 551–588.

Schäffer, H. A. and I. A. Svendsen (1988). Surf beat generation on a mild sloping beach. In *Proc. 21st Int. Conf. Coastal Eng.*, New York, pp. 1058–1072.

Symonds, G., D. A. Huntley, and A. J. Bowen (1982). Two dimensional surf-beat: Long wave generation by a time-varying break point. *Journal of Geophysical Research 87*, 233–244.

Thornton, E. B. and R. J. Calhoun (1972). Spectral resolution of breakwater reflected waves. *Journal ASCE Waterways Harbour and Coastal Engineering WW4*, 443–460.

Tucker, M. J. (1950). Surf beats: sea waves of 1 to 5 min. period. In *Proc. Roy. Soc. Lond. A*, pp. 565–573.

Van Dongeren, A. R. (1997). *Numerical modelling of quasi-3d nearshore hydrodynamics*. Phd dissertation, University of Delaware, Newark, DE.

Van Dongeren, A. R., H. J. Bakkenes, and T. T. Janssen (2002). Generation of long waves by short wave groups. In *Proc. 28th Int. Conf. Coastal Eng.*, Cardiff, pp. 151–164.

Van Dongeren, A. R. and I. A. Svendsen (1997). An absorbing generating boundary condition for shallow water models. *Journal of Waterway, Port, Coastal and Ocean Engineering 123*, 303–313.

Zelt, J. A. and J. E. Skjelbreia (1992). Estimating incident and reflected wave fields using an arbitrary number of wave gauges. In *Proc. 23rd. Int. Conf. Coastal Eng.*, pp. 777–789.

Appendix A

Wave envelope

To find an expression for the amplitude of a certain periodic function with amplitude a and frequency ω, $x(t) = a\cos\omega t$, we can see this as the real part of a so-called *analytical*, complex function $z(t)$,

$$\mathrm{Re}(z(t)) = x(t) = a\cos\omega t \qquad \text{with} \qquad z(t) = x(t) + iy(t). \tag{A.1}$$

A function $z(t)$ with the properties answering equation (A.1) is

$$z(t) = e^{i\omega t}, \tag{A.2}$$

with

$$\mathrm{Im}(z(t)) = y(t) = a\sin\omega t. \tag{A.3}$$

The imaginary part is nothing more than the original signal with a 90 degrees phase shift, so cosines become sines and vice versa. This shifted signal is called the Hilbert transform of a signal (for more information on Hilbert transform see section A.1). Since the amplitude of the Hilbert transformed signal equals the amplitude of the original signal, the analytical signal can be seen as a signal which 'stores surface elevation' in the imaginary part when the real part (the actual elevation) is not at its maximum value.

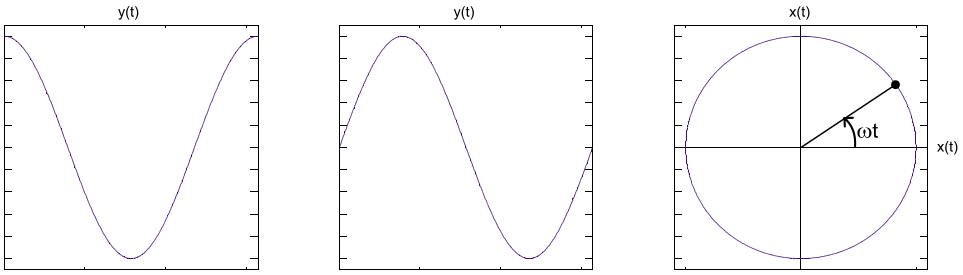


Figure A.1: Amplitude determination, Left panel: original signal, Middle panel: shifted signal, Right panel: amplitude graph.

Plotting $z(t)$ in the complex plane (see Figure A.1) it can easily be seen that the amplitude of the function

$x(t)$ is equal to the radius of the graph in the right pane

$$\sqrt{x^2(t) + y^2(t)} = \sqrt{a^2} = |a|, \tag{A.4}$$

which is quite obvious considering $x(t)$ itself. Since the wavefields concerned in this thesis are not single sines or cosines, the applicability of a Hilbert transform to obtain amplitude information of a Fourier transformed time-signal $\eta(t)$ is considered. Assume $\eta(t)$ to be the sum of a large number of cosines,

$$\eta(t) = \sum_{n=1}^{N} C_n \cos \omega_n t + \epsilon_n, \tag{A.5}$$

where C_n and ϵ_n represent the (real) amplitude and phase of component n respectively. Similar to the monochromatic case we can now define a function $z(t)$ answering

$$\mathrm{Re}(z(t)) = \eta(t), \tag{A.6}$$

namely

$$z(t) = \sum_{n=1}^{N} C_n e^{i(\omega_n t + \epsilon_n)}. \tag{A.7}$$

The imaginary part of (A.7) is the Hilbert transform of the original signal $\eta(t)$. Let $\eta(t)$ now be a narrow banded wave train ($|\omega_n - \omega_0| \ll \omega_0$), where ω_0 represents the dominant (or peak) frequency. In order to find an expression for the (now time-varying) amplitude $a(t)$ we factor out e^{ω_0},

$$z(t) = e^{i\omega_o t} \sum_{n=1}^{N} C_n e^{i((\omega_n - \omega_0)t + \epsilon_n)}. \tag{A.8}$$

With $z(t) = a(t)e^{i\omega_0 t}$ we can write for $a(t)$

$$a(t) = \sum_{n=1}^{n} C_n e^{i((\omega_n - \omega_0)t + \epsilon_n)}. \tag{A.9}$$

The (real) amplitude can finally be calculated from $|a(t)|$. Since the assumption of a narrow banded spectrum was adopted, (A.9) represents a slowly varying amplitude of the wave field. A broad spectrum would result in an envelope with frequency components equal to the components of the wave signal itself, in that case a Hilbert transformation does not add any information of use. Jonswap spectra are considered narrow-banded, so the Hilbert transform is applicable to those wavefields.

A.1 Hilbert transformation

In the previous section the Hilbert transformation is used to obtain amplitude information of a time-signal. Although the method is applicable for numerous frequency components, this section shows the Hilbert transform in the case where $\eta(t)$ is a bichromatic signal. The real and imaginary spectra are obtained by Fourier transforming $\eta(t)$ and shown in Figure A.2.
Multiplying these spectra by i and $-i$ for frequencies higher and lower than the Nyquist frequency respectively, the graphs shown in Figure A.2 change into the graphs shown in Figure A.3. The real parts become

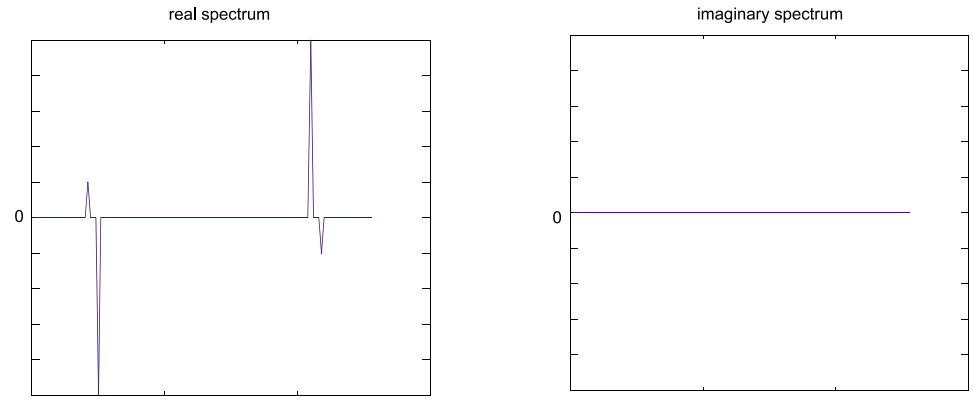


Figure A.2: Frequency spectra of bichromatic signal. Left panel: real parts, Right panel: imaginary parts.

imaginary and vice versa. The graphs represent the Fourier series of the shifted signal, so inverse Fourier transformation of the spectra shown in Figure A.3 yields the phase-shifted time series of the bichromatic signal. This signal is used as the imaginary part of the analytic signal $z(t)$ in the previous section.

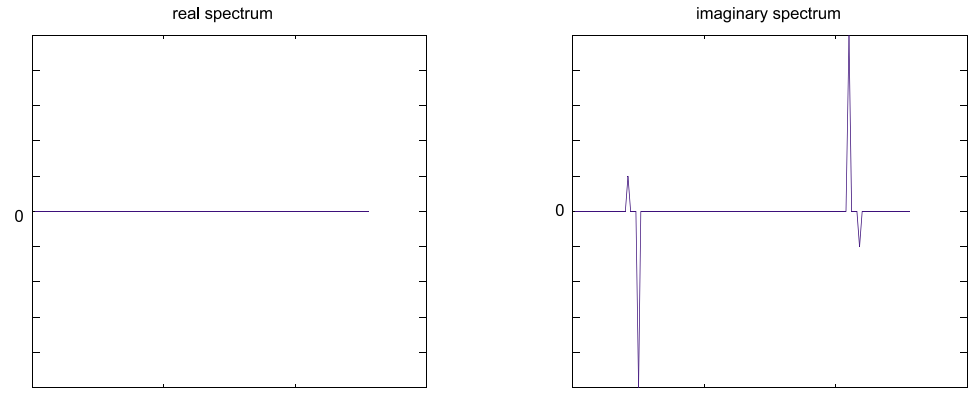


Figure A.3: Frequency spectra of shifted bichromatic signal. Left panel: real parts, Right panel: imaginary parts.

Appendix B

Windowing

Breaking down a time signal into frequency components, an exact transformation is only obtained when a set of rules following from the nature of Fourier analysis is obeyed. When a part $x(t)$ of an unlimited registration $v(t)$ of e.g. surface elevation with length T is taken for Fourier transformation, a so-called rectangular window is used implicitly. The formal definition of this window is

$$u_r(t) = \begin{cases} 1 & 0 \leq t \leq T \\ 0 & \text{otherwise} \end{cases} . \tag{B.1}$$

So the time series $x(t)$ can be considered as the product

$$x(t) = u_r(t)v(t). \tag{B.2}$$

The Fourier transformed window $u_r(t)$ is shown in Figure B.1. Its algebraic expression reads

$$U_r(f) = \mathscr{F}(u_r(t)) = T\left(\frac{\sin \pi f T}{\pi f T}\right) e^{-i\pi f T} \tag{B.3}$$

It can be seen from Figure B.1 (left panel), that on every integer multiple of $1/T$ the value of $|U_r(f)|$ is zero and therefore no leakage will occur for these frequencies. For the bi-chromatic waves the specific frequencies

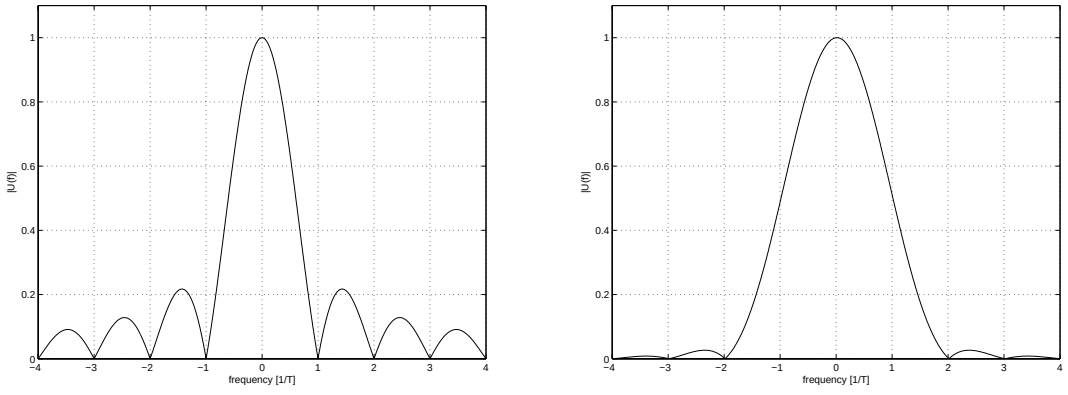


Figure B.1: Spectral windows for rectangular (left panel) and Hanning (right panel) time windows.

are at our disposal so this is an important phenomenon when determining the exact frequencies (a multiple of the basic frequency $1/T$), sample frequency f_s and duration of the time-record T. In the irregular case this is impossible since the spectrum of an irregular wave field is continuous over the frequency axis. However, a discrete Fourier Transform (DFT) is only able to transform a certain (discrete) signal into a discrete spectrum. In order to avoid the leakage to the sidelobes shown in Figure B.1 (left panel), a new window is introduced to replace the rectangular one. This is the so-called Hanning window

$$u_h(t) = \begin{cases} \frac{1}{2}\left(1 - \cos\frac{2\pi t}{T}\right) = 1 - \cos^2\left(\frac{\pi t}{T}\right) & 0 \leq t \leq T \\ 0 & \text{otherwise} \end{cases} \tag{B.4}$$

The Fourier transform of this window is plotted in Figure B.1 (right panel). Important differences with the rectangular window are the nonzero values in the adjacent frequencies $f = f + 1/T$ which is not desirable for the bichromatic case. The advantage of the Hanning window is the low leakage over the spectrum, indicated by the relative small side lobes compared to the rectangular lobes. For irregular tests therefore this Hanning window is usually applied.

Appendix C

Data acquisition

The present appendix discusses the system used for organizing data files and the processes used to convert them to Matlab-files.

C.1 Experiments

A signal, amplified by the gauge amplifier shown in Figure C.2, is transmitted to a so called *DAP-box*(see Figure C.3). This device samples the signal of all enabled channels with a fixed rate: 25 Hz. The sampled signal is stored by *DasyLab* software. Although many actions can be performed on the collected data within DasyLab, for safety reasons the raw sampled data is stored directly, without any operation performed. For every session a ASCII-file is created with a name like: `a-1_70_5.ASC` representing a test with parameters from series A-1, a water depth of 70 cm (which is actually redundant information) and the fifth file generated for series A-1. Including the series performed in the horizontal case, about 15 sessions are recorded for each individual series. Therefore the sequence counter is a hexadecimal counter for the convenience of having one character when importing files into Matlab. All separate session files are stored in folders named after the date the sessions were performed.

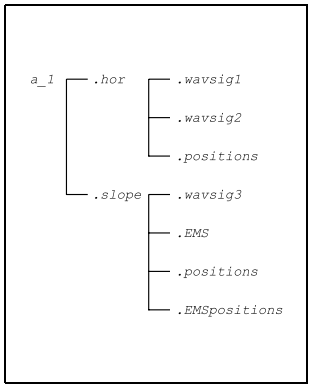


Figure C.1: Contents of structural array.

The conversion to Matlab-files is performed by a script named `dataimport.m` and makes use of several functions; `importhor.m` for the conversion of the horizontal tests; `combdata_???.m` where the question marks denote a specific series. This script combines the ASCII files obtained by the different session for every series. The gauging constants are used in `import_data.m` (subfunction of `combdata_???`) and `importhor.m`. The output of the `dataimport.m` script is 15 *mat*-files, one for every series. The variables stored in these files are *structural arrays*[1], having the properties shown in Figure C.1. The x coordinates of the gauge locations and the surface elevation is stored in meters ([m]), the EMS recordings are in Volts [V] and can be converted to [m/s] by the constant 10 [V/(m/s)].

hor.wavsig1 and hor.wavsig2 represent recordings of surface elevation taken in the horizontal case. The recordings per gauge are stored column-wise, the matrix size is therefore $[8192 \times 11]$. The locations of the gauges in the

[1] more information in Matlab help files



Figure C.2: 4 wave gauge amplifiers.

horizontal case are stored in hor.locations.
The slope.EMS variable consist 8 columns where the odd columns contain the vertical component recorded by the EMS and the even columns contain the horizontal velocity information. It is noted that in none of the recording-matrices a time column is present.



Figure C.3: Data acquisition hardware: computer(left) and 16-channel DAP-box (right).

location no.	1	2	3	4	5	6	7	8	9	10
x coordinate [m]	6	6.5	7	7.5	8	8.5	9	9.5	10	10.5
wave gauge	*	*	*	*	*	*	*	*	*	*
EMS										

location no.	11	12	13	14	15	16	17	18	19	20
x coordinate [m]	11	11.5	12	12.5	13	13.5	14	14.5	15	15.5
wave gauge	*	*	*	*	*	*	*	*	*	*
EMS	*									

location no.	21	22	23	24	25	26	27	28	29	30
x coordinate [m]	16	16.5	17	17.5	18	18.5	19	19.5	20	20.5
wave gauge	*	*	*	*	*	*	*	*	*	*
EMS	*									

location no.	31	32	33	34	35	36	37	38	39	40
x coordinate [m]	21	21.5	22	22.5	23	23.3	23.6	23.9	24.2	24.5
wave gauge	*	*	*	*	*	*	*	*	*	*
EMS	*									

location no.	41	42	43	44	45	46	47	48	49	50
x coordinate [m]	24.8	25.1	25.4	25.7	26	26.3	26.6	26.9	27.2	27.5
wave gauge	*	*	*	*	*	*	*	*	*	*
EMS							*			

location no.	51	52	53	54	55	56	57	58	59	60
x coordinate [m]	27.8	28.1	28.4	28.7	29	29.3	29.6	29.9	30.2	30.5
wave gauge	*	*	*	*	*	*	*	*	*	*
EMS										

location no.	61	62	63	64	65	66	67	68	69	70
x coordinate [m]	30.8	31.1	31.4	31.7	32	32.3	32.6	32.9	33.2	33.5
wave gauge	*	*	*	*	*	*	*	*	*	*
EMS										

location no.	71	72	73	74	75	76	77	78	79	80
x coordinate [m]	33.8	34.1	34.4	34.7	35	35.3	35.6	35.9	36.2	36.5
wave gauge	*	*	*	*	*	*	*	*	*	*
EMS										

Appendix D

Graphics

D.1 HF wave decomposition

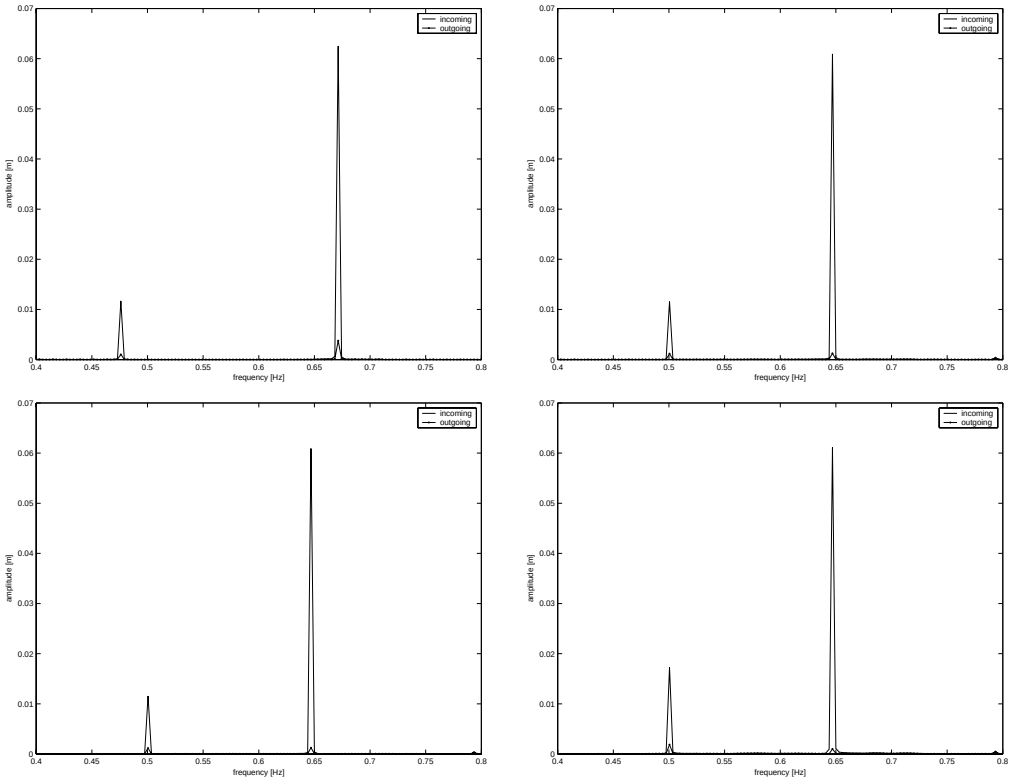


Figure D.1: Results of HF wave decomposition. Left column: series A. Right column: series B.

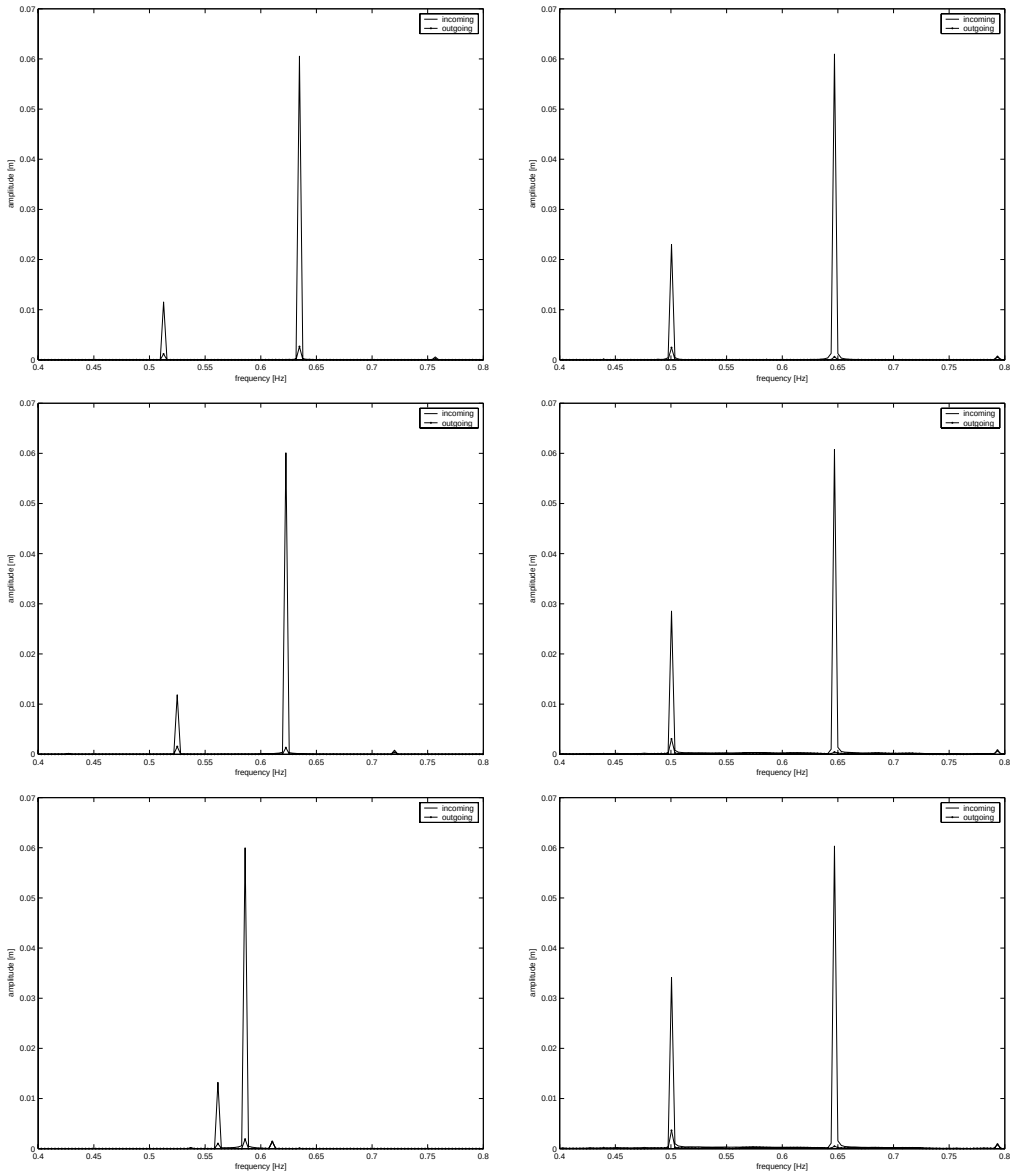


Figure D.2: Results of HF wave decomposition. Left column: series A. Right column: series B.

D.2 3-D representation of spatial evolution of amplitude spectra

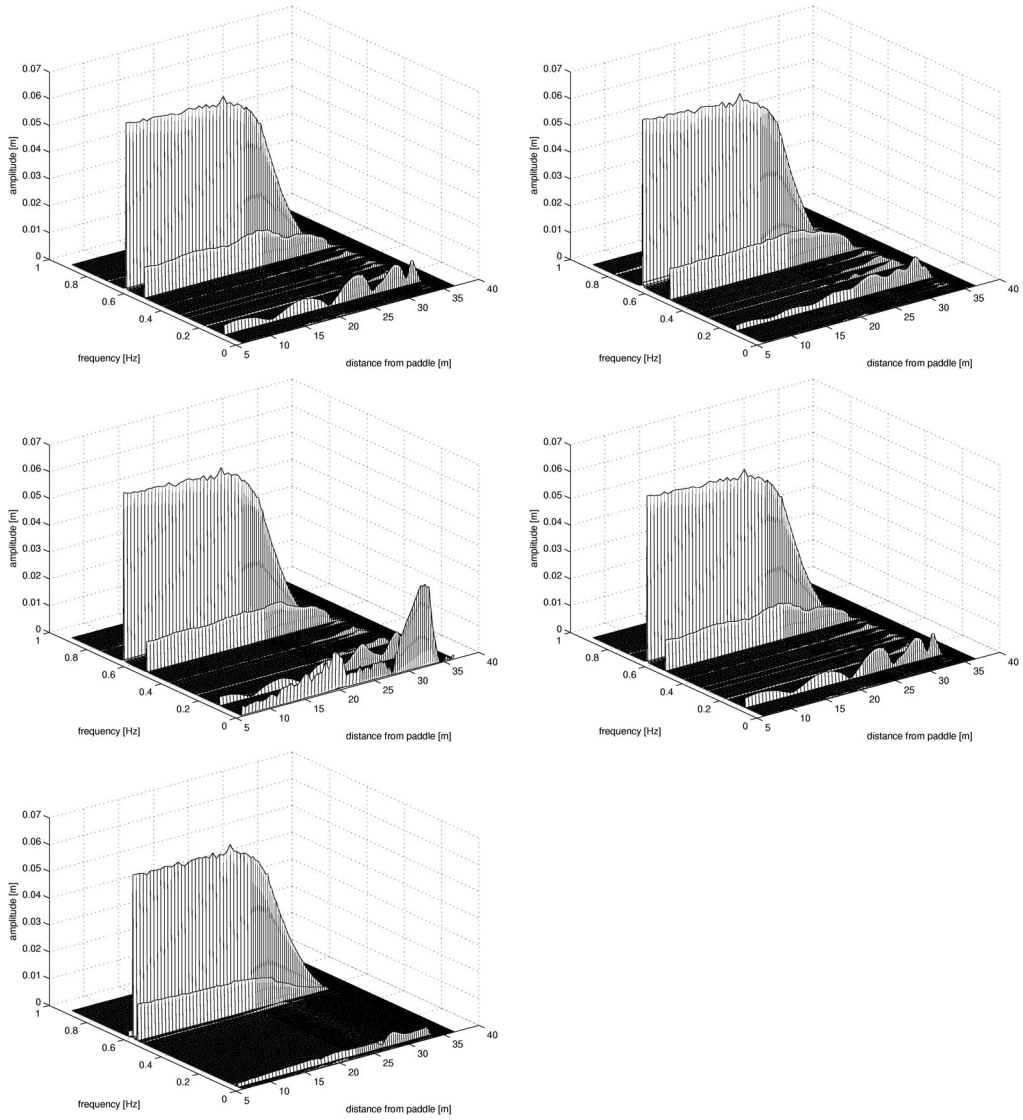


Figure D.3: 3-D amplitude spectra for series A.

D.3 Overview of analysis

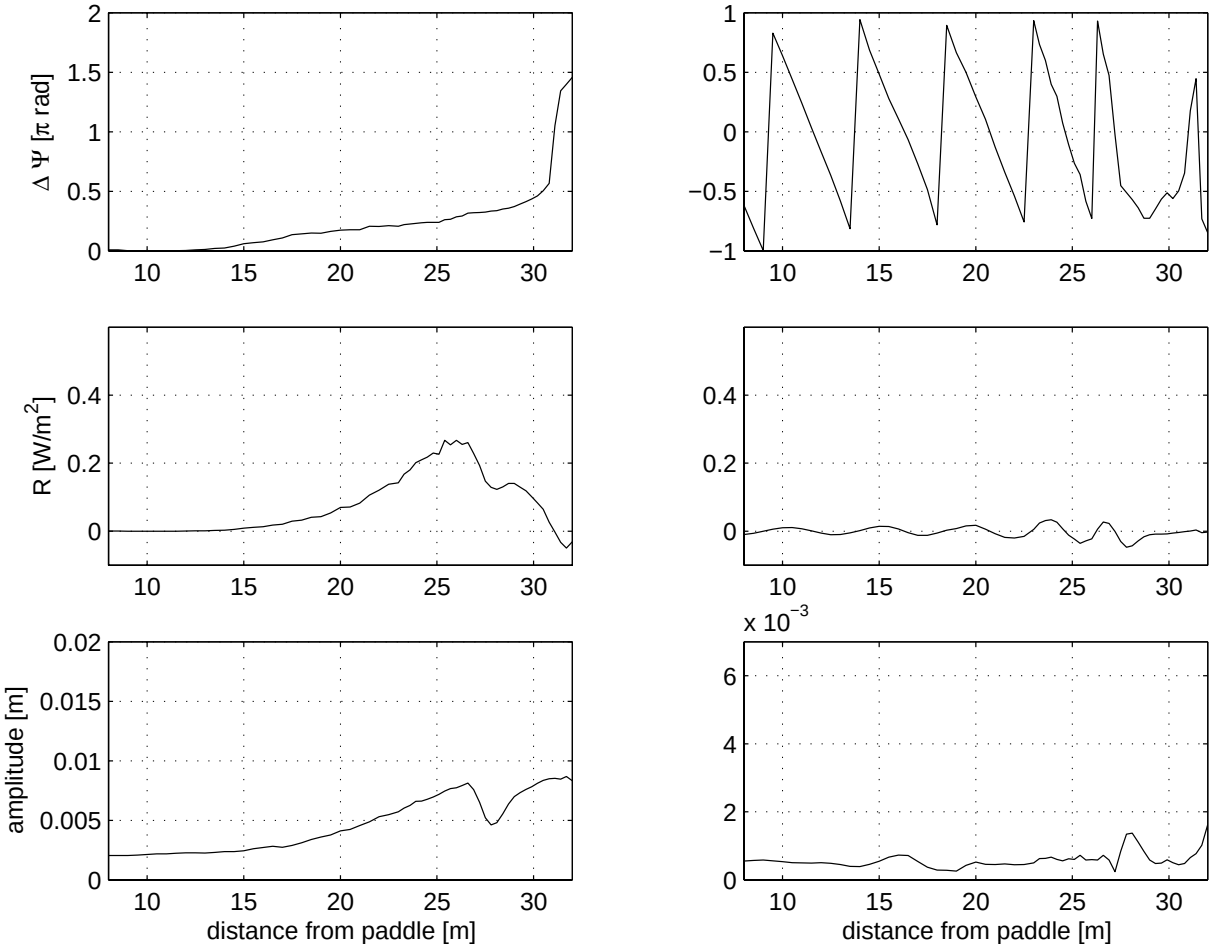


Figure D.4: Compilation of series A-1, Top row: phase lag. Middle row: transferred energy. Bottom row: amplitude. Left column incoming waves. Right column: outgoing waves.

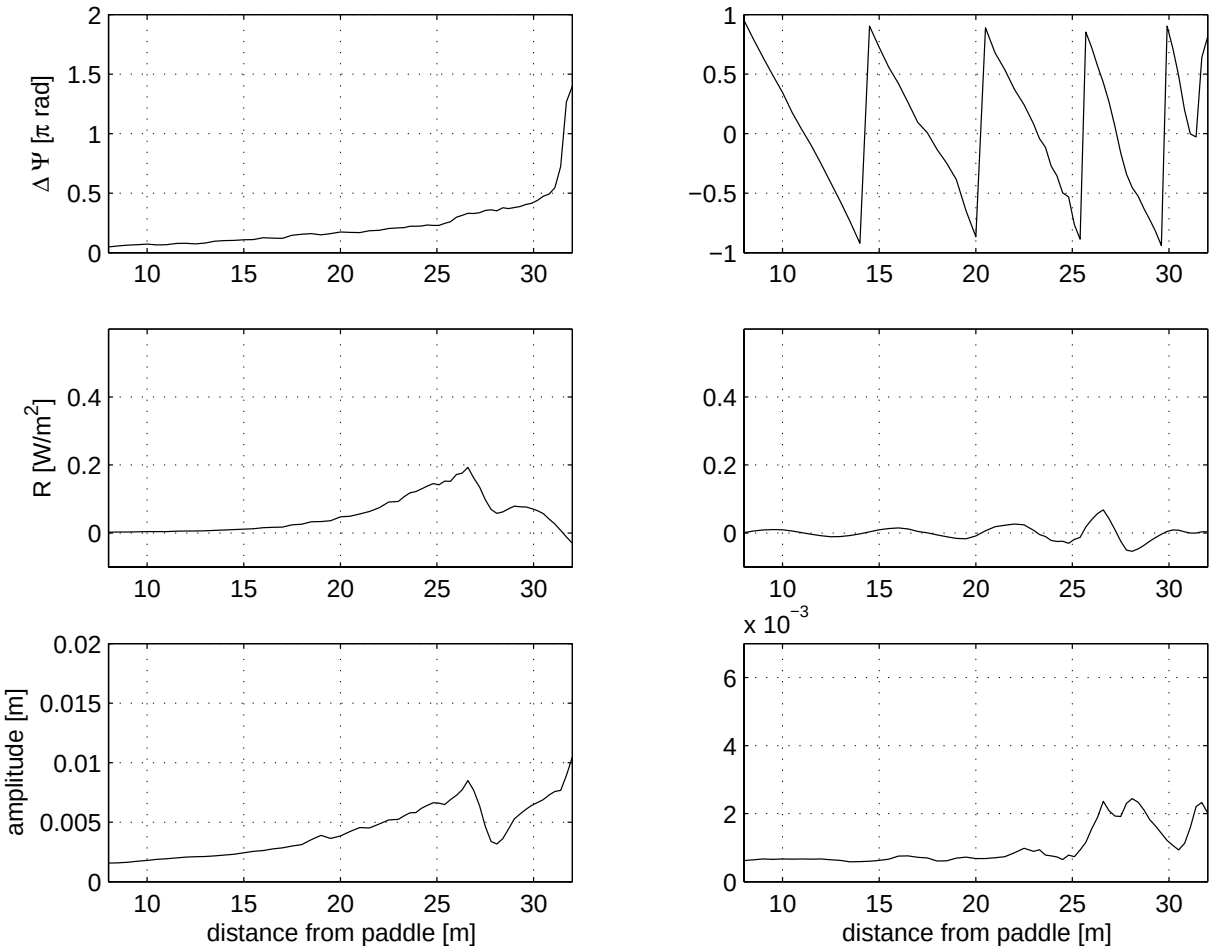


Figure D.5: Compilation of series A-2, Top row: phase lag. Middle row: transferred energy. Bottom row: amplitude. Left column incoming waves. Right column: outgoing waves.

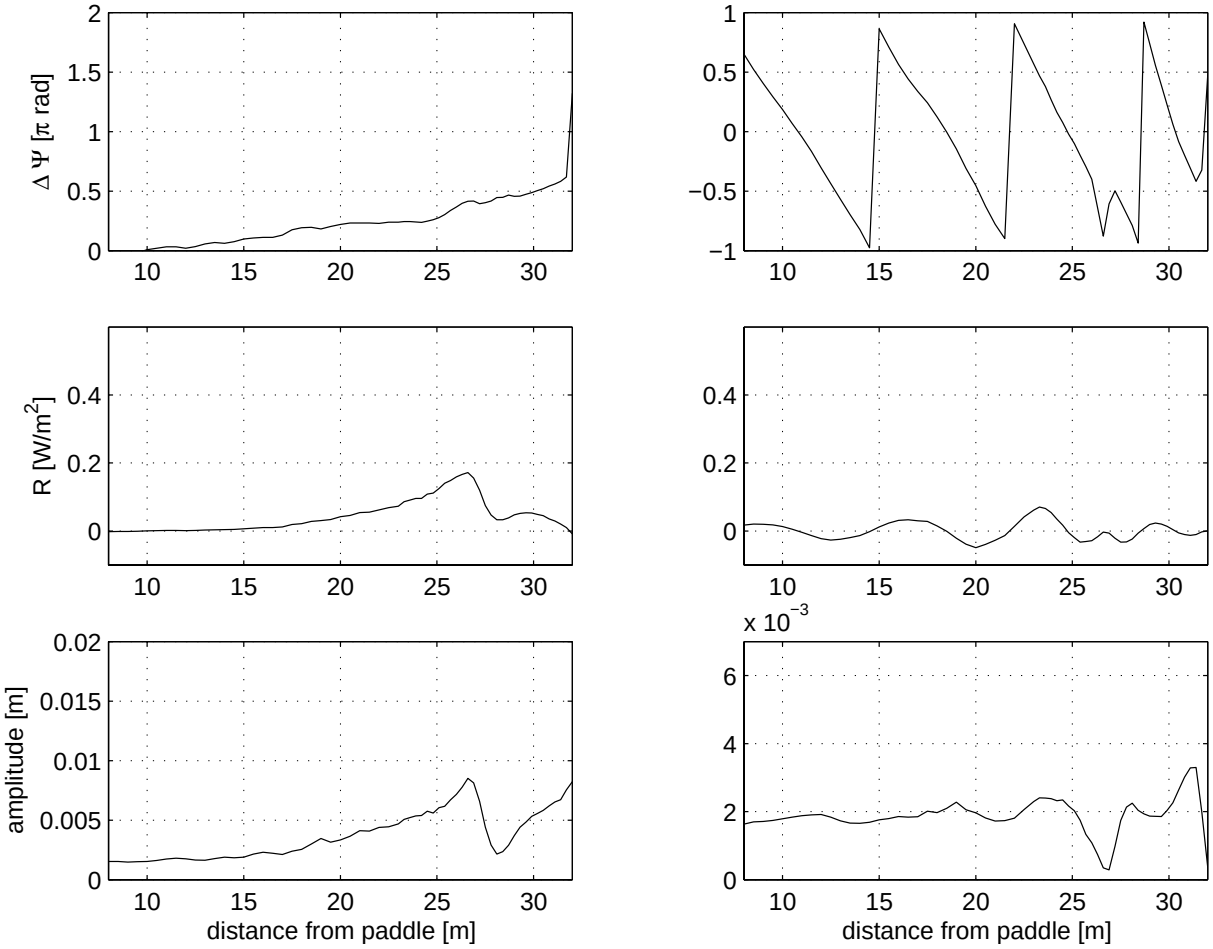


Figure D.6: Compilation of series A-3, Top row: phase lag. Middle row: transferred energy. Bottom row: amplitude. Left column incoming waves. Right column: outgoing waves.

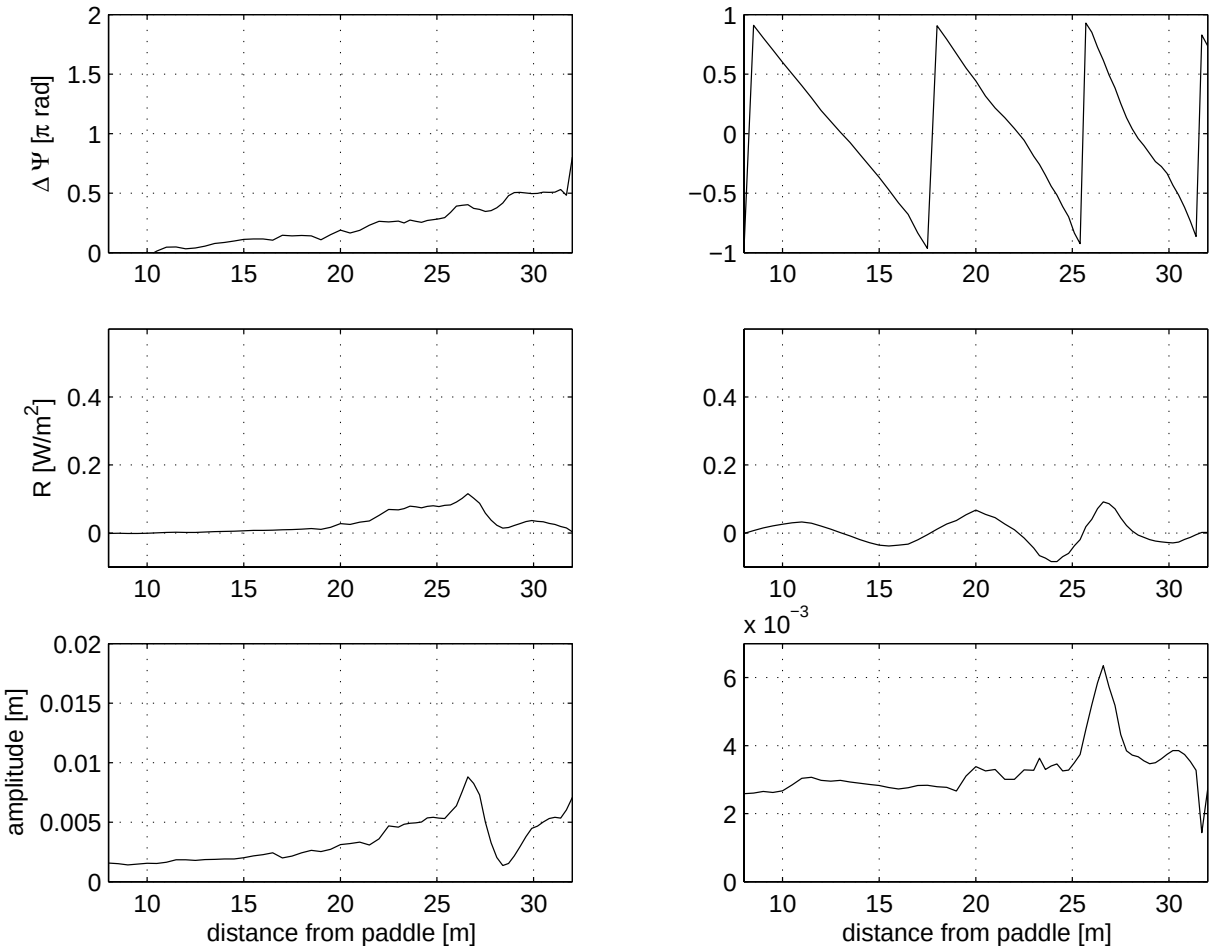


Figure D.7: Compilation of series A-4, Top row: phase lag. Middle row: transferred energy. Bottom row: amplitude. Left column incoming waves. Right column: outgoing waves.

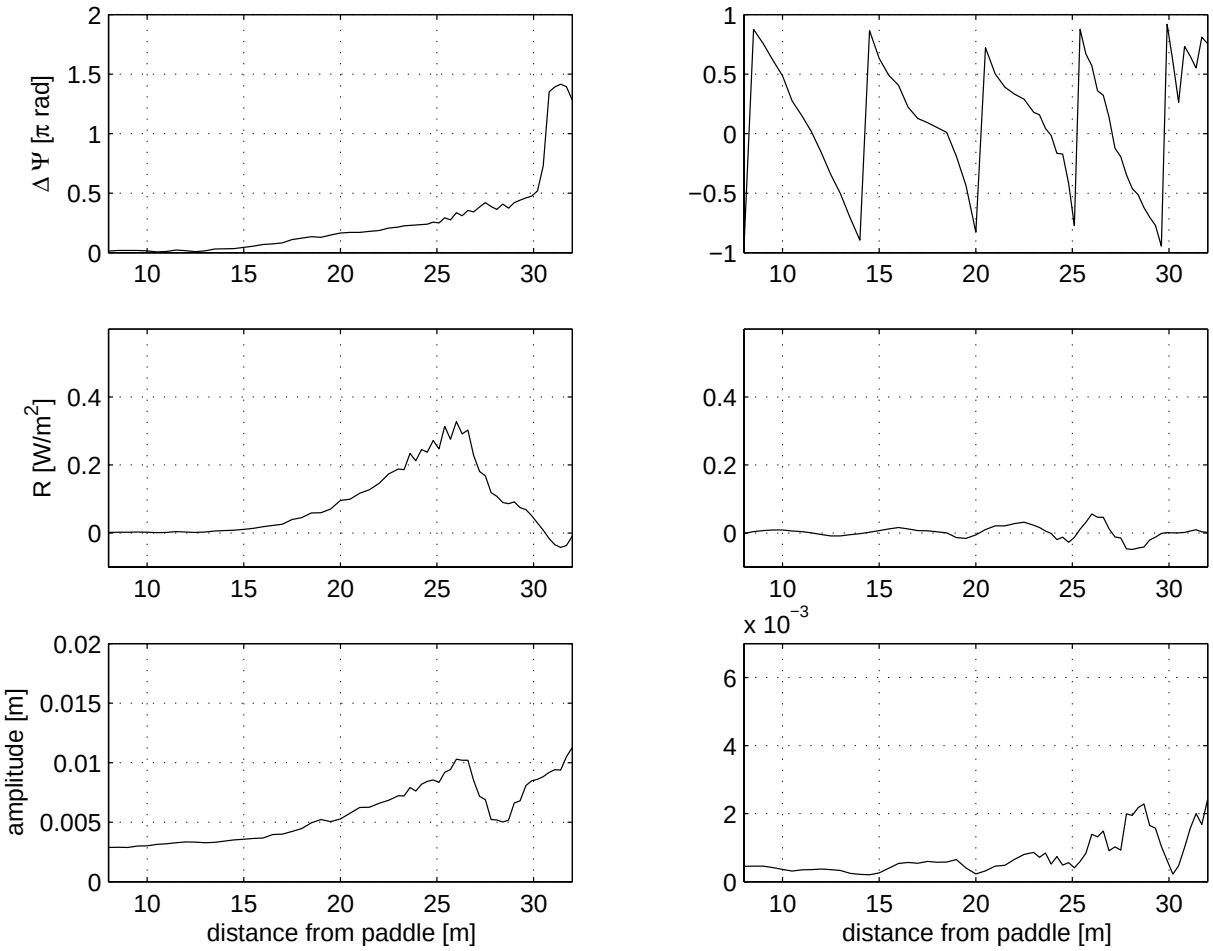


Figure D.8: Compilation of series B-2, Top row: phase lag. Middle row: transferred energy. Bottom row: amplitude. Left column incoming waves. Right column: outgoing waves.

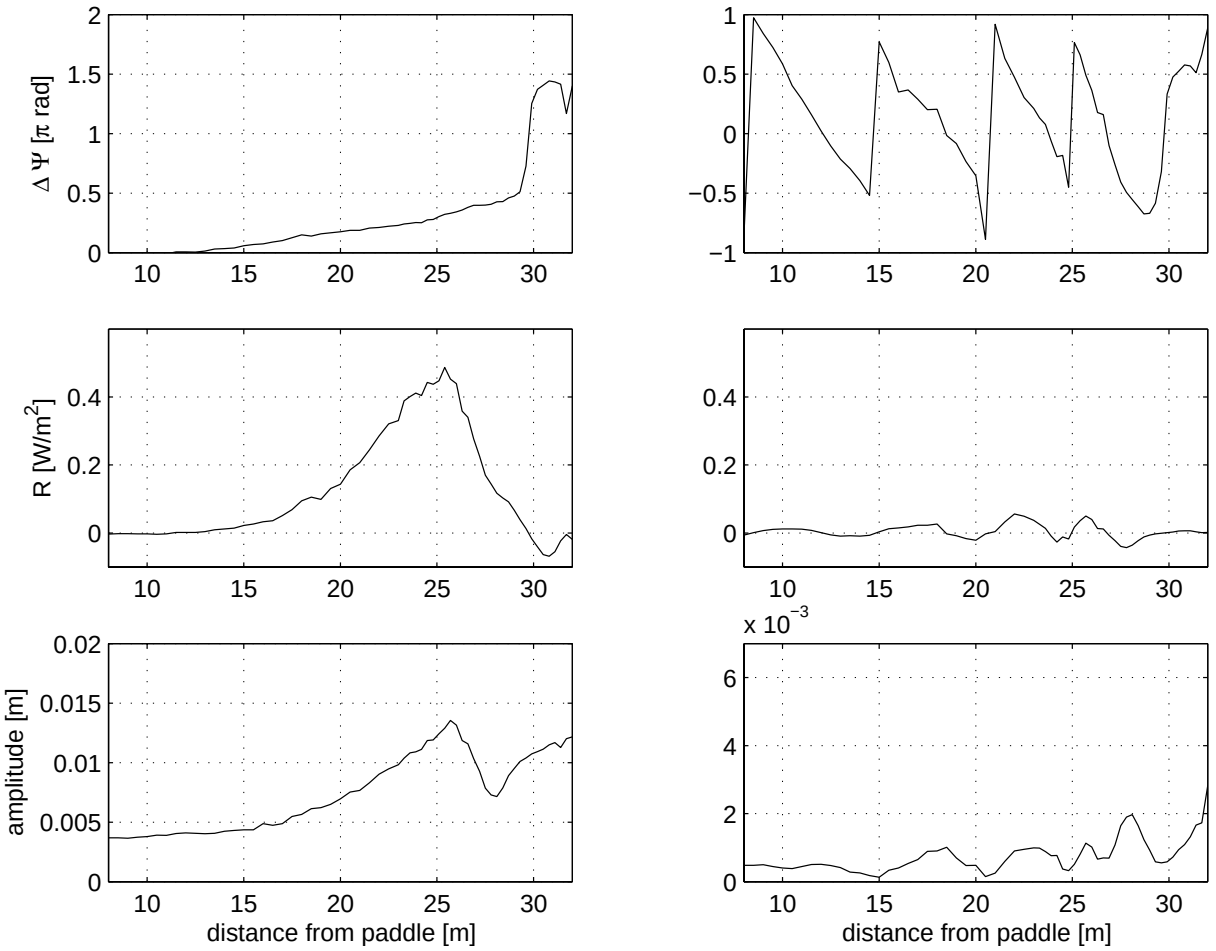


Figure D.9: Compilation of series B-3, Top row: phase lag. Middle row: transferred energy. Bottom row: amplitude. Left column incoming waves. Right column: outgoing waves.

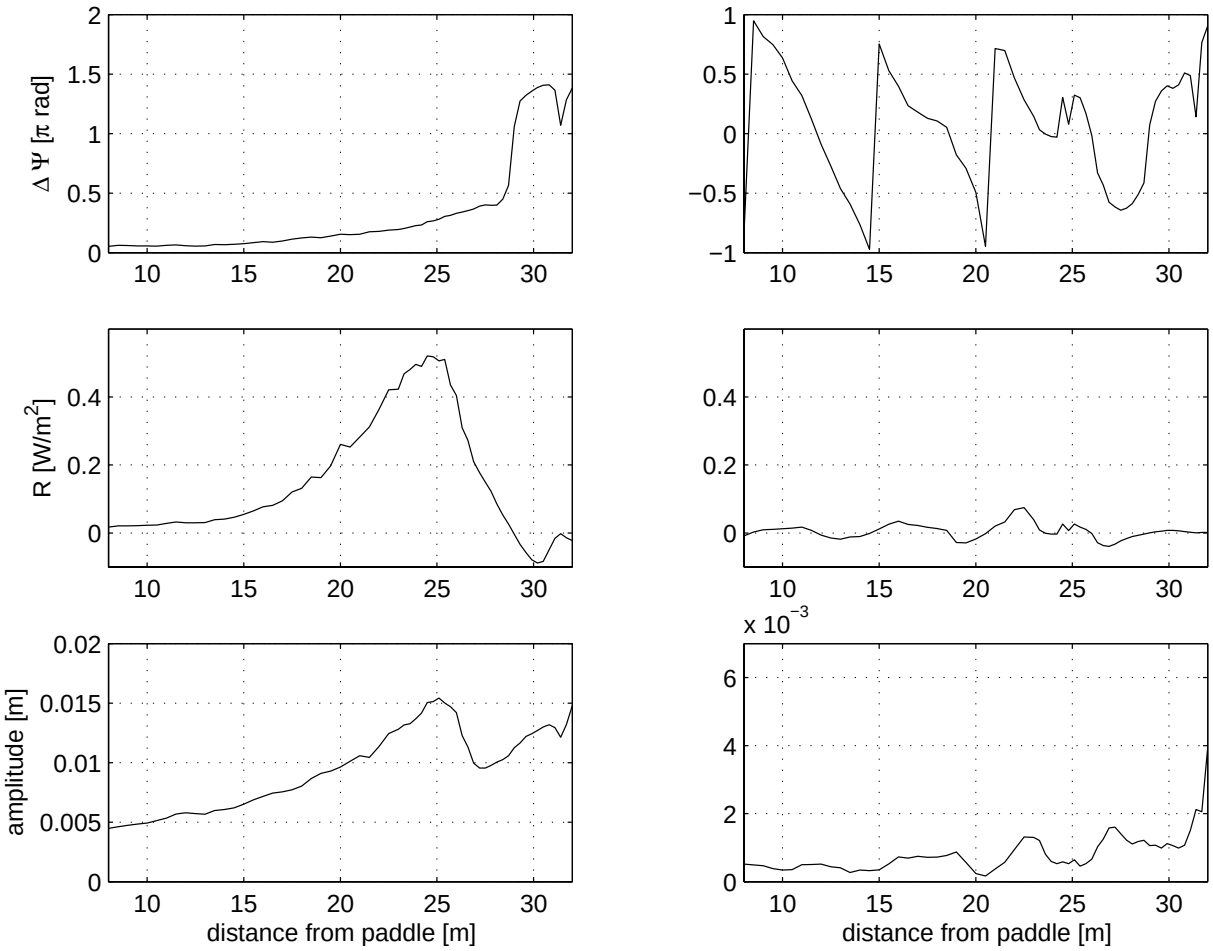


Figure D.10: Compilation of series B-4, Top row: phase lag. Middle row: transferred energy. Bottom row: amplitude. Left column incoming waves. Right column: outgoing waves.

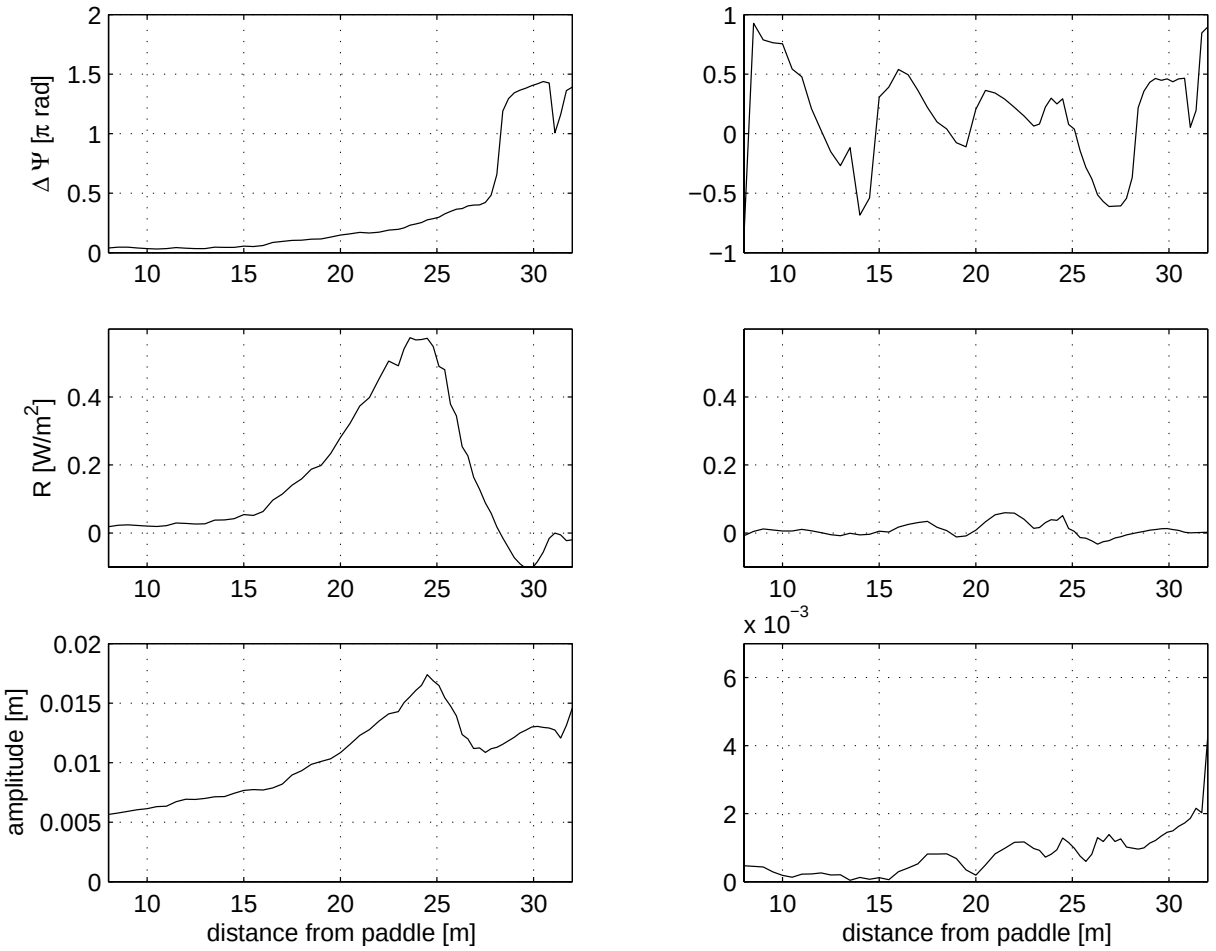


Figure D.11: Compilation of series B-5, Top row: phase lag. Middle row: transferred energy. Bottom row: amplitude. Left column incoming waves. Right column: outgoing waves.

D.4 Reflection plots

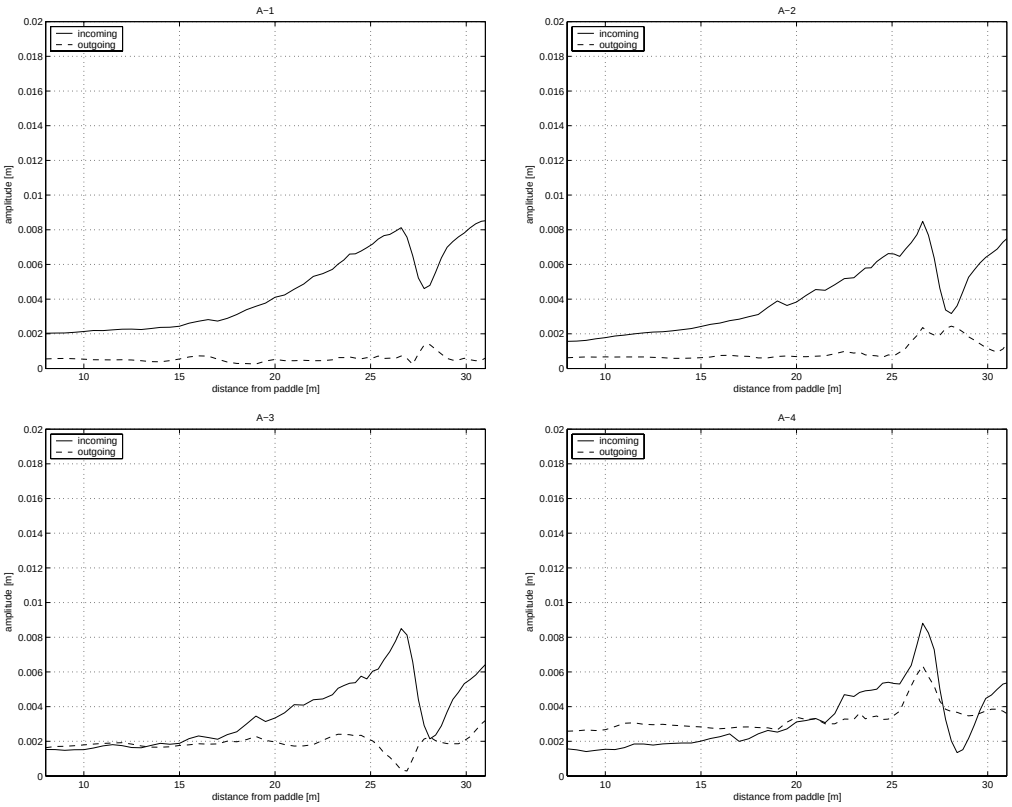


Figure D.12: Incoming and outgoing amplitude for series A-1 trough A-4.

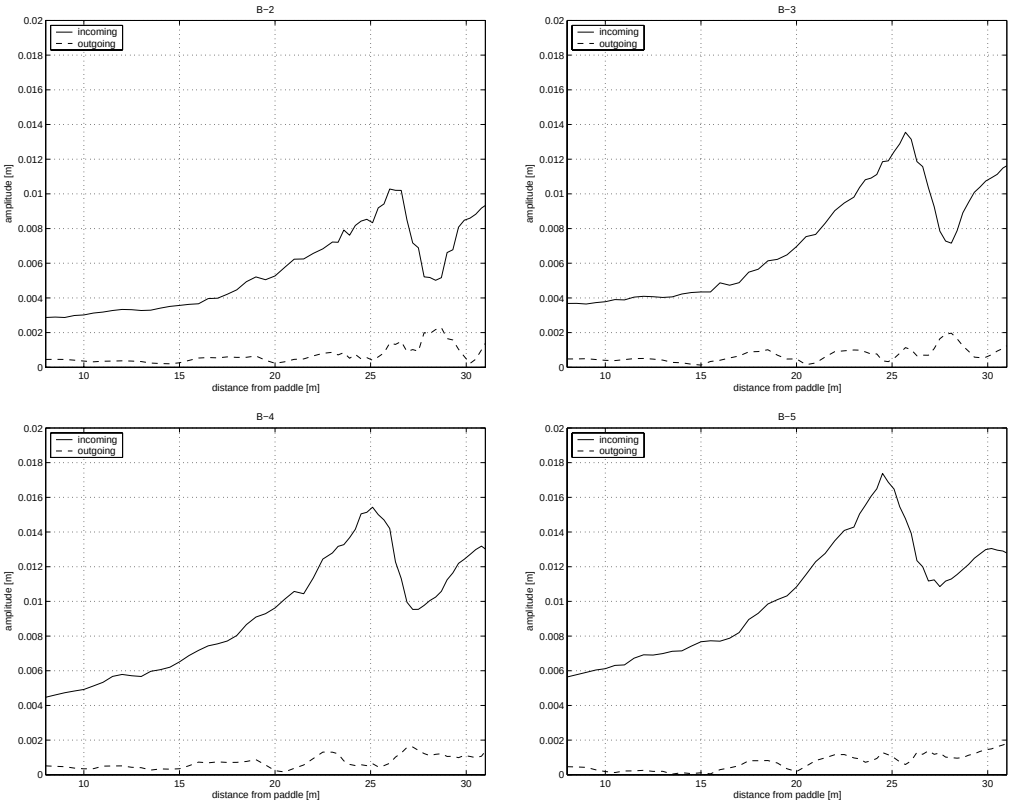


Figure D.13: Incoming and outgoing amplitude for series B-2 trough B-5.